

Bayesian Statistics as a New Tool for Spectral Analysis: I. Application for the Determination of Basic Parameters of Massive Stars

J.-M. Mugnes^{*} and C. Robert

Département de physique, de génie physique et d'optique, Université Laval, and Centre de Recherche en Astrophysique du Québec, Québec, Canada

ABSTRACT

Spectral analysis is a powerful tool to investigate stellar properties and it has been widely used for decades now. However, the methods considered to perform this kind of analysis are mostly based on iteration among a few diagnostic lines to determine the stellar parameters. While these methods are often simple and fast, they can lead to errors and large uncertainties due to the required assumptions.

Here we present a method based on Bayesian statistics to find simultaneously the best combination of effective temperature, surface gravity, projected rotational velocity, and microturbulence velocity, using all the available spectral lines. Different tests are discussed to demonstrate the strength of our method, which we apply to 54 mid-resolution spectra of field and cluster B stars obtained at the Observatoire du Mont-Mégantic. We compare our results with those found in the literature. Differences are seen which are well explained by the different methods used. We conclude that the B-star microturbulence velocities are often underestimated. We also confirm the trend that B stars in clusters are on average faster rotators than field B stars.

Key words: massive stars, B stars, spectral analysis, Bayesian statistics

1 INTRODUCTION

Massive stars are bright and short-lived objects. Therefore they are relatively easy to observe and remain close to their birth place. Their influence on their environment is important, from photoionizing HII regions, polluting their environment with enriched chemical elements, to expelling material out of galaxies. But they also represent an important candidate, due to their high level of internal radiation pressure, for the general study of stellar evolution. Therefore an accurate characterization of the fundamental and spectral parameters of massive stars is greatly needed in astrophysics.

One of the most useful tools to investigate massive stars is quantitative spectroscopy, which involves the comparison of a stellar spectrum with synthetic data created by state-of-the-art atmospheric models. There is a wide variety of comparison technics presented in the literature. But whether it is by fitting spectral lines “by eye” (Searle et al. 2008), by using χ^2 minimization (Daflon et al. 2007), or by measuring equivalent widths (Lefever et al. 2010), most of these methods rely on an iterative process, due to the large number of parameters involved in the analysis. For B stars, these

parameters are the effective temperature T_{eff} , the surface gravity $\log(g)$, the projected rotational velocity $v \sin(i)$, the micro- and macro-turbulence velocity ξ and ζ , and of course the abundances of the chemical elements. The iterative analysis usually starts by adopting best-estimate values for all parameters. It then alternatively refines each parameter individually while using specific spectral indicators that are mostly sensitive to a sub-sample of parameters. For instance, in B stars the hydrogen lines $H\beta$ and $H\gamma$ are mostly sensitive to T_{eff} and $\log(g)$, while ionized silicon lines are mostly sensitive to T_{eff} , ξ , and its abundance. Therefore, one can start by assuming initial values for T_{eff} , $\log(g)$, and ξ for instance, and then use the Balmer lines to determine a new $\log(g)$ value. This new result combined with the Si lines is then used to infer a new effective temperature and, going back to the Balmer lines, to update $\log(g)$, and so on until all the parameter values are stable. Of course, this does not mean that each indicator is completely insensitive to the other parameters. On the contrary, there is a highly non-trivial coupling between all the involved parameters (Nieva & Przybilla 2010). And due to this coupling, the use of an iterative process based on a few spectral indicators can lead to a local solution rather than a global solution that takes into account all the parameters (Mugnes & Robert 2012).

^{*} E-mail: jmmugnes@gmail.com

Moreover, depending on the diagnostic lines used and on the initial parameter values, the same method may not give the same results. Also, due to the large number of parameters involved and in order to reduce computation time, many works in the literature have focused on a reduced number of parameters while assigning fixed values for the others (for instance by adopting solar abundance values, or assuming $\xi = 2 \text{ km s}^{-1}$ for main sequence stars and 10 km s^{-1} for evolved stars). Fixed values are often based either on theoretical estimates or on results from other works. For example, Searle et al. (2008) used the projected rotational velocities of Howarth et al. (1997). But as discussed in the present work, the final results depend on the choice of the parameter that is fixed and on the choice of the value adopted. Even for a given atmospheric model and a given set of observed spectra, all the simplifications done (i.e. the adoption of initial estimated values, the use of fixed parameters, or an iterative process with only a few specific indicators for a reduced number of parameters) have an impact on the results and their accuracy and make it difficult to compare or to compile results from different works in a consistent way. It is therefore important to find a method which does not rely on initial estimations of the parameters, that will simultaneously constrain all the parameters using most of (if not all) the available information contained in an observed spectrum, and will work in a reasonable amount of time.

Thanks to the development of computer power, along with its recent success in many scientific fields, Bayesian statistic has been more and more used in astrophysics during the last decades. Studies found in the literature cover a large range of astrophysical topics, from redshift estimations with photometry (Benítez 2000) to the study of magnetic fields in interstellar clouds (Crutcher et al. 2010), including cosmological parameter selection (Trotta 2007). Among these studies, a few authors applied Bayesian statistics to the determination of stellar parameters, hereby illustrating some of its advantages. For instance Pont & Eyer (2004) used Bayesian statistics to redefine the age-metallicity relation in field dwarfs. They showed that most of the scatter found in the previously derived age-metallicity relation was due to a simplified treatment which, among other issues, did not properly take into account systematic biases. Shkedy et al. (2007) performed a complex and complete study of the impact of both systematic and statistical measurement errors on stellar parameters and their uncertainties. More recently, Schönrich & Bergemann (2014) developed a method which allow the combined use of photometric, spectroscopic, and astrometry informations for the determination of stellar parameters and metallicities. Nevertheless, none of these studies were applied on massive stars, nor did they performed a spectral analysis involving more than three parameters at the same time (the spectroscopic part of the work of Schönrich & Bergemann 2014 focused only on the effective temperature, surface gravity, and global metallicity).

In this work, we use both a large pre-calculated grid of synthetic spectra and small interpolated and tailored grids in order to reduce the computation time. Bayesian statistics are applied to allow for a logical and numerical connection between the two grids as well as to constrain all the parameters at the same time while using nearly all the available information given by a spectrum. In the present paper, as a way to introduce our method and to illustrate the param-

eter interdependency, we focus on four stellar parameters (effective temperature, surface gravity, projected rotational velocity, and microturbulence velocity). In a following paper, we will add individual chemical abundances and the global metallicity to the analysis.

The next section summarises the ingredients and vocabulary used in Bayesian statistics. This is followed by a description of our technic and different tests done to demonstrate its reliability. stellar parameters are obtained for a sample of B stars and are compared to other works.

2 DESCRIPTION OF THE METHOD

We here briefly describe the key elements of Bayesian statistics involved in our method. For a complete description of Bayesian statistics see Gregory (2010).

2.1 The Bayes Theorem

2.1.1 Definition

Let us make an experiment or an observation that allow us to retrieve some data D (a stellar spectrum for instance) in order to test a given hypothesis H (for example, the hypothesis that a given atmospheric model reproduce correctly the stellar spectrum). And let us also assume that we have some prior knowledge or information I (the stellar parameters given by an approximate spectral type for instance). Then by using the Bayes theorem we can assign a plausibility degree (or probability) to the hypothesis H . Namely, the Bayes theorem states that the probability P of H being true given D and I is called the posterior probability and is given by:

$$P(H|D, I) = \frac{P(H|I) * P(D|H, I)}{P(D|I)}, \quad (1)$$

where $P(H|I)$ is the prior probability which is obtained over a previous set of data or from previous knowledge, $P(D|H, I)$ is the likelihood, i.e. the result of the actual data D , and where the global likelihood $P(D|I)$ is a normalization factor. Simply put, according to the Bayes theorem, our final state of knowledge (the posterior probability) is the product of what we already knew (the prior probability) with what the experiment (the likelihood) tells us.

2.1.2 Application to a Stellar Spectrum

In this work we adapt the Bayes theorem to stellar spectroscopy considering three main concepts :

- 1) Let us consider an observed spectrum of a given star that contains several spectral lines. We then artificially divide the whole spectrum into smaller spectra, each centered on an individual spectral line (Fig. 1a). Each smaller spectrum can be seen as an individual observation. As the original spectrum can be described as a data set D composed of all the spectral resolution elements (or flux points) contained in the whole spectrum, then each smaller spectrum k can also be described as a data set D_k composed of all the spectral resolution elements contained in the spectrum k (Fig. 1b). Thus for a given star, we have K independent spectra, where each spectrum k is centered on the spectral line k and is

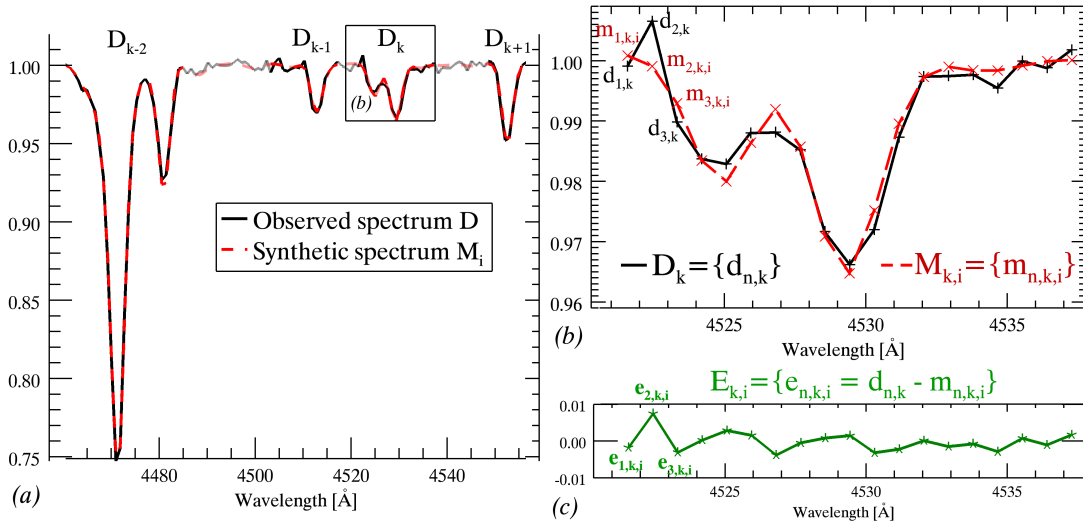


Figure 1. Illustration of the data sets. (a): Superposition of an observed spectrum D (black) and synthetic spectrum M_i (dashed red). Lighter parts of the spectra are not considered in the analysis. (b): Close up of one sub-spectrum D_k where each observed and synthetic spectral resolution elements are labeled $d_{n,k}$ and $m_{n,k,i}$, respectively, with n ($1 \leq n \leq N_k$) the number of resolution elements in D_k , k ($1 \leq k \leq K$) the number of sub-spectra, and i ($1 \leq i \leq Nb_{model}$) the number of synthetic spectra. (c): Errors $e_{n,k,i}$, assuming that the observed spectrum is defined as $d_{n,k} = m_{n,k,i} + e_{n,k,i}$.

described by a data set D_k (where $1 \leq k \leq K$, and K is the total number of lines contained in the original observed spectrum).

2) As we want to fit an observed spectrum over a grid of synthetic spectra, we can replace the hypothesis H by a set of hypothesis M_i (with $i = 1, 2, \dots, Nb_{model}$) representing the propositions stating that each *synthetic spectrum calculated with an atmosphere model M with a set of parameters i is true* (i.e. correctly reproduces the observation). Then for a given data set D_k , we can assign a probability for each synthetic spectrum. Since the propositions M_i are mutually exclusive, we can write : $\sum_i P(M_i|D, I) = 1$.

3) Finally each line k (or experiment k) has an associated prior information I_k and a posterior probability reflecting our state of knowledge respectively before and after doing the experiment k .

We can then rewrite the Bayes theorem for each line k as :

$$P(M_i|D_k, I_k) = \frac{P(M_i|I_k) * P(D_k|M_i, I_k)}{P(D_k|I_k)}. \quad (2)$$

If we use the posterior probability given by the line $k-1$ as the prior probability of the line k , then we can define the prior information of the line k with $I_k = D_{k-1}, I_{k-1}$ (i.e. the combined information given by the previous data set D_{k-1} , or line $k-1$, and its associated prior information I_{k-1}). The Bayes theorem then becomes:

$$P(M_i|D_k, I_k) = \frac{P(M_i|D_{k-1}, I_{k-1}) * P(D_k|M_i, I_k)}{P(D_k|I_k)}, \quad (3)$$

which can be understood as: the probability that the synthetic spectrum M_i reproduce well the observed line D_k is proportional to the quality of the fit (likelihood) between the observed line D_k and the corresponding synthetic line from the spectrum M_i times the probability that the same synthetic spectrum M_i reproduce the previous line D_{k-1} with the previous corresponding synthetic line.

Here $P(M_i|D_k, I_k)$ is the posterior probability for one synthetic spectrum M_i . When we consider all the synthetic spectra at the same time, $\{P(M_i|D_k, I_k)\}_{i=1..Nb_{models}}$ is thus called the posterior probability distribution (the same obviously applies for the likelihood and the prior).

In other words, if we apply this theorem to all the lines in the observed spectrum (each time using the last posterior probability distribution as a prior for the next line) and considering all the synthetic spectra, we obtain, in the end, a final posterior probability distribution that simultaneously takes into account all the constraints given by all the lines in the observed spectrum for all the considered parameters. Figure 2, shows an example of the process when we apply our method on 4 spectral lines using 25 synthetic spectra. Note here that the order of the lines to which we apply the theorem does not matter. Indeed, if we neglect the normalisation factors, the final posterior probability is simply the product of the first prior probability with the likelihoods of all the lines involved.

2.1.3 Constructing the Likelihood

In order to construct a proper likelihood, we need to make a few basic assumptions. First, each data set D_k (i.e. line k) is composed of N_k independent spectral resolution elements $D_k = \{d_{n,k}\} = d_{1,k}, d_{2,k}, \dots, d_{N_k,k}$ (Fig. 1b). Then we can do the same for the model spectrum $M_{i,k} = \{m_{n,k,i}\} = m_{1,k,i}, m_{2,k,i}, \dots, m_{N_k,k,i}$ (Fig. 1b). Finally let us suppose that each observed spectral resolution element can be associated with a spectral resolution element from a model, given a certain flux error $d_{n,k} = m_{n,k,i} + e_{n,k,i}$ (Fig. 1c). If we suppose the errors $\{e_{n,k,i}\}$ to be independent and represented by a Gaussian distribution centered on zero with a standard deviation of $\sigma_{n,k}$, then we can write the likelihood as:

$$\begin{aligned}
P(D_k|M_i, I_k) &= \prod_{n=1}^N \left[\frac{1}{(\sqrt{2\pi}\sigma_{n,k})} \right] * \\
&\exp \left[-\sum_n \frac{(d_{n,k} - m_{n,k,i})^2}{2\sigma_{n,k}^2} \right] \\
&= C_k \exp \left[-\frac{\chi_{i,k}^2}{2} \right]. \quad (4)
\end{aligned}$$

The errors can represent the noise in the data but also the incompleteness of the model (due to simplifications, approximations, or unknown variables) or even some errors in the reduction process of the data (bad normalisation for instance). To take these sources into account, we define the standard deviation of the gaussian distribution as follow:

$$\sigma_{n,k} = \sqrt{(\sigma_{noise})_{n,k}^2 + (\sigma_{model})_{n,k}^2}, \quad (5)$$

where $(\sigma_{noise})_{n,k}$ refers to the errors coming from the noise in the data, and $(\sigma_{model})_{n,k}$ refers to the other sources of errors (model incompleteness and reduction errors). In this work, for simplicity, we assume $(\sigma_{noise})_{n,k} = \sigma_{noise}$, a constant for all the spectrum, defined as the standard deviation in regions of the normalised continuum of the observed spectrum. And for each line, $(\sigma_{model})_{n,k}$ is given by:

$$\begin{aligned}
(\sigma_{model})_{n,k} &= \min_{\forall i} \left(\sqrt{\frac{1}{N_k} \sum_n (d_{n,k} - m_{n,k,i})^2} \right) \\
&= (\sigma_{model})_k. \quad (6)
\end{aligned}$$

In other words, for each line k , $(\sigma_{model})_k$ is the minimal RMS between the observed line and all the corresponding model spectrum $M_{i,k}$. With these definitions, $\sigma_{n,k}$ is the same for all the spectral resolution elements n of a line, but is different for each line. Thus:

$$\sigma_{n,k} = \sqrt{\sigma_{noise}^2 + (\sigma_{model})_k^2} = (\sigma_\chi)_k. \quad (7)$$

Note that $(\sigma_\chi)_k$ is a very important variable as it ultimately links physical imperfections and theoretical incompleteness to the uncertainty of the final parameters. And with this decomposition, if we were to work with perfect data ($\sigma_{noise} \rightarrow 0$), then the uncertainty of the final parameters would be related to the limitations of the atmospheric or atomic models used. Inversely, if we have a perfect model ($(\sigma_{model})_k \rightarrow 0$), the final uncertainties would then be directly related to the quality of the data.

2.1.4 Global Likelihood and First Prior

Now, since $\sum_i P(M_i|D_k, I_k) = 1$, the global likelihood $P(D_k|I_k)$ is then given by:

$$P(D_k|I_k) = \sum_i (P(M_i|D_{k-1}, I_{k-1}) * P(D_k|M_i, I_k)). \quad (8)$$

And the Bayes theorem (Eq. 3) becomes:

$$\begin{aligned}
P(M_i|D_k, I_k) &= \frac{P(M_i|D_{k-1}, I_{k-1}) * C_k \exp \left[-\frac{\chi_{i,k}^2}{2} \right]}{\sum_i \left(P(M_i|D_{k-1}, I_{k-1}) * C_k \exp \left[-\frac{\chi_{i,k}^2}{2} \right] \right)}. \quad (9)
\end{aligned}$$

Finally, when we apply the theorem (Eq. 9) for the first time, we assume that all models M_i are equiprobable: $P(M_i|D_0, I_0) = 1/Nb_{model}$ (i.e. we consider a flat prior distribution as in Fig. 2c, and D_0 represents no data). This means that, at first, we do not give preference to any model (or set of parameters). Note here that we are not performing a model comparison but a parameter estimation and as we use large data samples, the results are not affected by the choice of the prior (Gregory 2010).

2.2 Parameter Estimation

In this work we focus on the stellar parameters T_{eff} the effective temperature, $\log(g)$ the surface gravity, $v \sin(i)$ the projected rotational velocity, and ξ the microturbulence velocity. We thus need to retrieve, from the final posterior probability mentioned above, an estimation for each parameter by considering all the other parameters. For this, we use another major feature of the Bayesian statistics, the marginalization. This is done by defining the model M_i as: *the synthetic spectrum computed with the model M using the set of parameters $T_{eff,i}$, $\log(g)_i$, $v \sin(i)_i$, and ξ_i* , which we write $M_i = T_i, l_i, v_i, \xi_i, M$. Since we suppose our model M to be true, our posterior probability thus becomes:

$$P(M_i|D_k, I_k) = P(T_i, l_i, v_i, \xi_i|M, D_k, I_k), \quad (10)$$

which can be read as the joint probability for T_i , l_i , v_i , and ξ_i to be true if the model M , the data D_k , and our prior knowledge I_k are true.

Since our parameters have discrete values in our analysis, we can retrieve the marginal posterior probability distribution for each parameter by using the marginalization equation. Here we give an example for T_i :

$$P(T_i|M, D_k, I_k) = \sum_a \sum_b \sum_c P(T_i, l_a, v_b, \xi_c|M, D_k, I_k), \quad (11)$$

which is the marginal probability distribution of T_i considering all the values of the other parameters. As shown in Figure 3, from this distribution we obtain the most probable value and the mean value, as well as the associated uncertainties which are defined as the values between which the sum of the marginal posterior probability distribution is equal to or greater than a certain confidence level $C = \sum_{T_-}^{T_+} P(T_i|M, D_k, I_k)$. In this work we use $C = 0.99$ which can be seen as a 3σ uncertainty (recall that $\sum_i P(T_i|M, D_k, I_k) = 1$). Note that these uncertainties are related to the variations of the other parameters but also, as stated in §2.1.3, to possible data or model imperfections.

2.3 Preventing Numerical Biases

Due to the fact that we want to treat all available lines equally, we need to calculate the χ^2 for the same number of spectral resolution elements in each line. Otherwise, broad features (such as hydrogen and helium lines in B stars) will dominate the solution over the narrow features (metal lines for instance) in the posterior probability.

Indeed, given the same differences $d_{n,k} - m_{n,k,i}$ between the observed and synthetic line and the same σ_χ for both a broad and a narrow line, only the number of spectral resolution elements will have an impact on the χ^2 value. The more

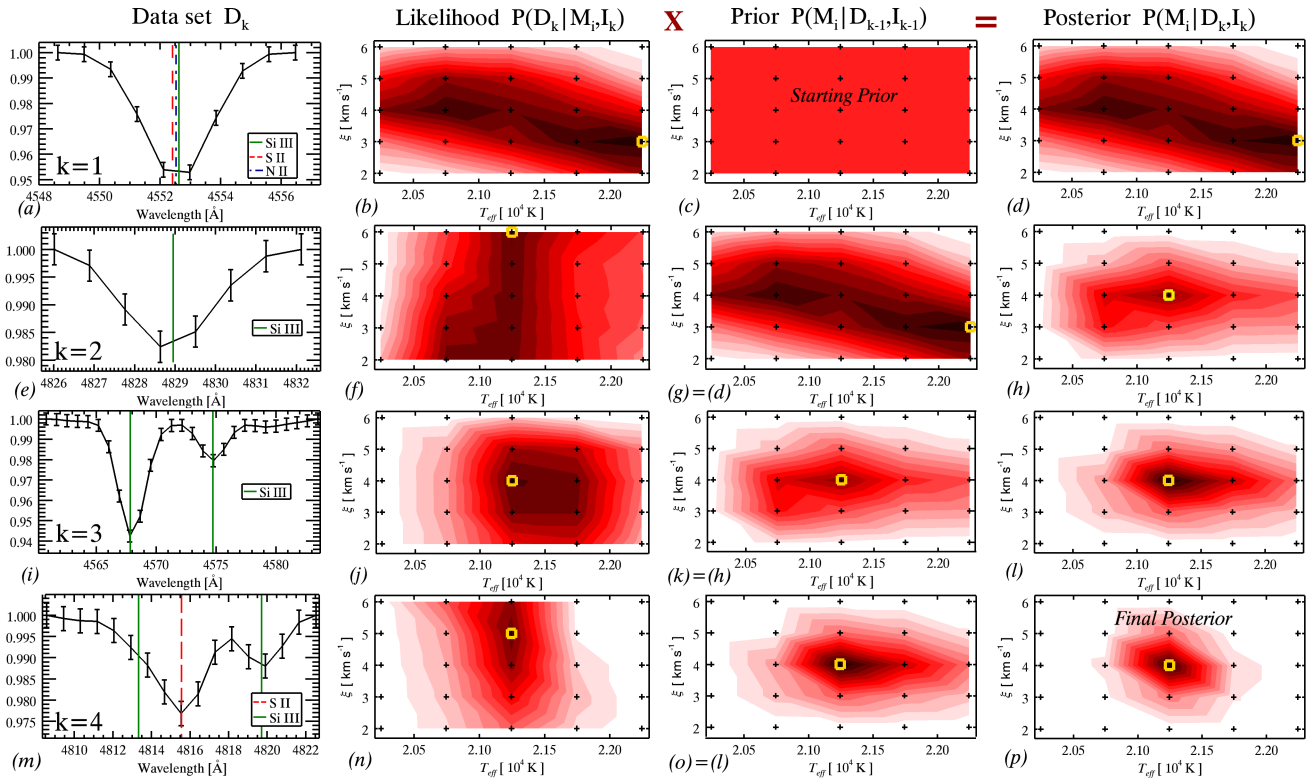


Figure 2. Illustration of the Bayesian analysis step by step. For this example, we consider 4 data sets (or lines) D_k and 25 synthetic spectra calculated with only two free parameters: T_{eff} and ξ . The black plus signs in columns 2, 3, and 4 indicate the value used for these two parameters. The colour of the surface contours is scaled to the relative probability of each distribution: the dark red regions being the most probable and the white ones the less probable. The yellow squares indicate the global maximum of each distribution. The first column shows every data set considered, and the second column the likelihood obtained for each data set as in Equation 4. The third column represents the prior probability distribution known at each step k , and the last column shows the posterior probability distribution which is the normalised product of the prior and the likelihood of a given step k . The method goes as follow: considering the first line $k = 1$ (in (a)), we calculate its likelihood using Equation 4 (in (b)), and use, as a first prior, a flat distribution (in (c)) assuming we have no knowledge of the best pair $[T_{eff}, \xi]$. We then apply the Bayes theorem (Eq. 3) and obtain the first posterior probability distribution (in (d)). For the next data set ($k = 2$), we perform the same operation but we use the posterior distribution of the previous step (in (d)) as a new prior distribution (in (g)) since our “state of knowledge” has been changed after the first step. In the end, the final posterior probability distribution (in (p)) represents the solution combining all the information given by the 4 lines. Note that since the method can be summarized as a series of products, the order in which we consider the data sets have no influence on the shape of the final posterior distribution (see Fig. A1).

spectral resolution elements there are, the higher is the value of the χ^2 . Therefore, the χ^2 of a broad line will rapidly increase and hence its likelihood will also rapidly tend to zero as the models differ from the solution, whereas a narrow line will see its likelihood slowly reach zero. Consequently when multiplying the prior probability density given by the broad line with the likelihood of the narrow line, only the broad line solution survives. To prevent this effect, we therefore interpolate each line with the same number of flux points given by the broadest line in the sample. This interpolation will obviously oversample the narrow lines, but it is a good way to consider each line equally without losing information (since interpolating each line with the number of flux points given by the narrowest line would imply a loss of detail in the broader lines). The oversampling has also the advantage of giving a more realistic weight to the narrow and weaker lines; the parameter space for the solution of a weaker line is then better defined.

2.4 Synthetic Spectra

We use atmospheric models from the metal line-blanketed, NLTE, plane-parallel, and hydrostatic code TLUSTY (Lanz & Hubeny 2007). With these models, we create synthetic spectra by running the program SYNPEC. More precisely, we use the SYNLOT package generously offered to us by Hubeny and Lanz, which contains a TLUSTY pre-calculated B-star grid (*BSTAR2006*) and the latest version of SYNPEC and SYNLOT which allows the user to interpolate more specific models from the closest *BSTAR2006* models. The *BSTAR2006* grid considers 16 values of the effective temperature, between 15000 K and 30000 K with a 1000 K step; 13 surface gravities, from 1.75 to 4.75 in $\log(g)$ with a step of 0.25 dex; and 6 chemical compositions, $Z/Z_\odot = 2, 1, 1/2, 1/5, \text{ and } 1/10$ (where Z_\odot is the solar composition); a solar helium abundance, $\text{He}/\text{H} = 0.1$ by number, and a microturbulence velocity of 2 and 10 km s^{-1} .

For this paper we consider only the solar chemical composition, as established by Asplund et al. (2009), and we

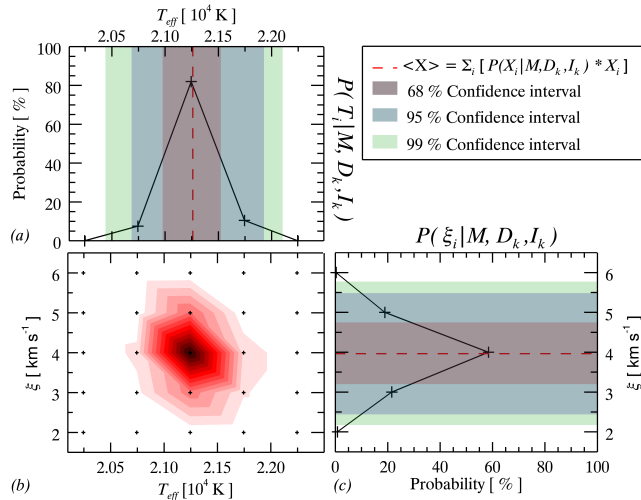


Figure 3. Examples of the marginal probability distribution for T_{eff} and ξ . These distributions (in (a) and (c)) are derived from the final posterior probability distribution (in (b)) taken from Figure 2p. The coloured regions in (a) and (c) indicate the 68%, 95%, and 99% confidence intervals which can be seen as a 1σ , 2σ , and 3σ uncertainties for the best value of each parameter. The dashed red lines show the position of the mean value of each parameter defined as $\langle X \rangle = \sum_i X_i * P(X_i | M, D_k, I_k)$, where X is one of the considered parameters. Since the parameter space is discrete, the most probable value found for a parameter might not be the true value but the closest value used in the calculation of the spectra. Thus the mean value can be a better estimation of the real value of a parameter.

use SYNPEC to create a grid of synthetic spectra (hereafter called *BaseGrid*) with the same values of the effective temperature and surface gravity as those of the *BSTAR2006* grid with an extended range of 7 microturbulence velocities, from 0 to 30 km s^{-1} with a step of 5 km s^{-1} . We then convolve these spectra to take into account rotational broadening with 21 different values of $v \sin(i)$, from 0 to 400 km s^{-1} with a 20 km s^{-1} step, to create our starting grid for the analysis: *BSTART*. Note that the spectra of *BaseGrid* are not convolved with instrumental and rotational broadening and are used, in this work, as the basis for the creation of a new spectrum or new refined grids by directly interpolating the non-convolved spectra (because this is faster than interpolating the *BSTAR2006* models) to the desired values of T_{eff} , $\log(g)$, and ξ .

For each star, we begin, as previously mentioned, by assuming a uniform prior probability over all the *BSTART* models. We then apply our Bayesian analysis over all the selected lines in the spectrum of a star using all the models of the *BSTART* grid. This first analysis gives us, after marginalization, a reduced parameter space by excluding all values outside the 99% confidence level. We then construct a refined grid in this new parameter space and we reanalyze the lines assuming, once more, a flat prior. The result gives an even more restricted parameter space over which we reconstruct another refined grid and redo the analysis, and so on. The program stops either when the parameter space remains unchanged or when the parameter steps used to create a new grid are equal to or smaller than a certain limit. Here, as a compromise between accuracy and com-

puting time, we set this limit at 100 K in T_{eff} , 0.03 dex in $\log(g)$, 5 km s^{-1} in $v \sin(i)$, and 1 km s^{-1} in ξ .

3 TESTING THE METHOD ON ARTIFICIAL STELLAR SPECTRA

As a way to test the efficiency of the method as well as its robustness to noise and uncertainties, we perform three tests.

For the first test, we create an artificial observational spectrum using synthetic spectra with the following specifications: $T_{eff} = 21350 \text{ K}$, $\log(g) = 3.80$, $v \sin(i) = 45 \text{ km s}^{-1}$, $\xi = 6 \text{ km s}^{-1}$, and solar chemical composition. The spectrum is also convolved with a Gaussian instrumental profile with a full width at half maximum (FWHM) of 2.3 \AA . Random noise is also added in order to emulate a standard deviation, σ_{noise} , that is typical of what we see in our actual observations (with $\sigma_{noise} \simeq 0.004$ in the normalised flux). Then, we compare the artificial spectrum with our models using the method described in §2.4. But, as we are in the situation of a perfect model and imperfect data, we set $(\sigma_{model})_k$ to 0 and we substitute σ_{noise} by $x\sigma_{noise}$ where $x = 1, 2, 3, \dots$ in Equation 7. This way, while not changing the actual noise level in the spectrum, we can overestimate its value in the calculation by increasing x , and thus, we can test the robustness of the method to noise over-estimation. This analysis is then repeated 10 times, each time increasing x by 1. The results are summarized in Figure 4.

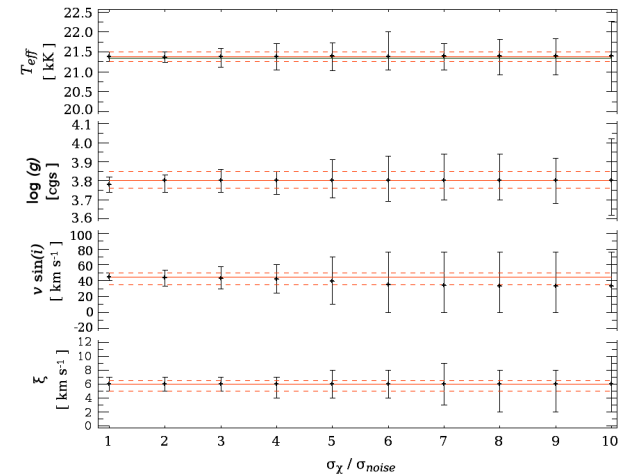


Figure 4. Plot of the stellar parameter values for 10 runs with increasing $\sigma_\chi / \sigma_{noise}$. Individual points and error bars are the results of the different runs. The green lines show the real parameter values used to create the artificial stellar spectrum ($T_{eff} = 21350 \text{ K}$, $\log(g) = 3.80$, $v \sin(i) = 45 \text{ km s}^{-1}$, and $\xi = 6 \text{ km s}^{-1}$). The orange lines show the results (full lines) and the corresponding uncertainties (dashed lines) from the analysis of the artificial spectrum without noise added and for $\sigma_\chi / \sigma_{noise} = 1$. The orange lines often overlap with the green lines.

While running the analysis on the artificial spectrum without noise added (orange lines in Fig. 4), the program returns almost the exact parameter values used to create this artificial spectrum (green lines in Fig. 4). There is only a slight difference of 10 K for the effective temperature which

is well under our minimal uncertainty (100 K). The runs for different values of $\sigma_\chi/\sigma_{noise}$ then give parameter values which are all very close to the original values used to create the artificial spectrum.

Increasing the ratio $\sigma_\chi/\sigma_{noise}$ means overestimating the noise level in the artificial spectrum, which should logically lead to greater parameter uncertainties since σ_χ acts as a tolerance parameter. Here, the parameter uncertainties increase with σ_χ roughly as $\sigma_{noise}/2$, as shown in Figure 5. This means that even when increasing the flux uncertainty by a factor of 2 or 3, there will be nearly no incidence on the method accuracy. Note also that, up to $4\sigma_{noise}$, the accuracy of $v \sin(i)$ is largely higher than the adopted resolution (around 77 km s^{-1} for a FWHM of 2.3 \AA). Usually, with classical methods, the uncertainty for $v \sin(i)$ with a value smaller than half the FWHM should be of the order of FWHM/2 since instrumental broadening becomes more important than rotational broadening under this limit. These effects are a direct consequence of cumulating the information from one line to the others and thus having multiple simultaneous constraints on each parameter. Note that when we use large σ_χ values, we find the classical uncertainties (close to the $v \sin(i)$ value when $v \sin(i)$ is below the classical limit) since, with such a huge tolerance parameter, most of the constraints coming from the lines disappears.

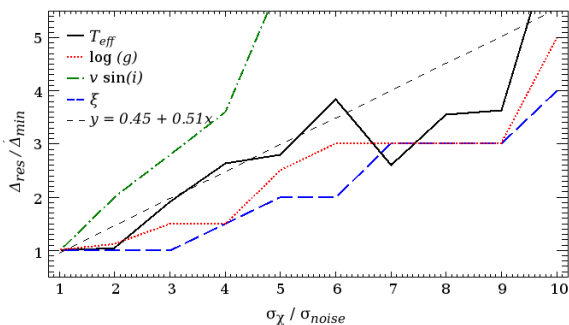


Figure 5. Plot of the relative stellar parameter uncertainties $\Delta_{res}/\Delta_{min}$ with increasing $\sigma_\chi/\sigma_{noise}$. For each parameter, Δ_{res} is the length of the error bars from Figure 4 and Δ_{min} the length of the smallest error bar found for the 10 runs. The thin black dashed line is a linear fit of the mean of all the parameter uncertainties.

Since spectral analysis usually tends to be more difficult and less accurate for fast rotating stars due to the blending of multiple lines, we repeat the first test for a higher projected rotational velocity, $v \sin(i) = 145 \text{ km s}^{-1}$. All the other parameters are unchanged (we are using the same lines as well for this analysis). The evolution of the parameter uncertainties is shown in Figure 6. Here, the effect seen in Figures 4 and 5 for a low $v \sin(i)$ value (compared to the instrumental FWHM) disappears while the slope of the fit shown in Figure 6 remains the same as in Figure 5. Also, the uncertainties of each parameter are of the same order as those obtained for a slow rotator. As this result is the same for an even faster rotator (for instance $v \sin(i) = 300 \text{ km s}^{-1}$), we can conclude that a faster rotational velocity does not affect the accuracy on the other stellar parameters when using our method. Again this is a consequence of cumulating the information from one line to the others.

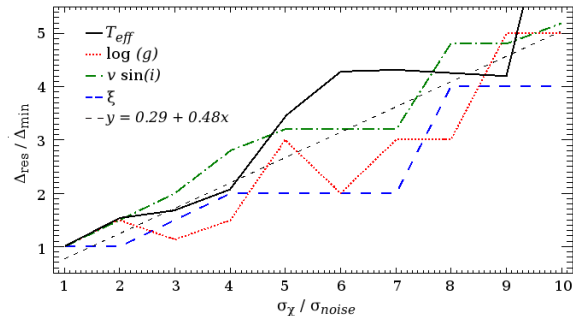


Figure 6. Plot of the relative stellar parameter uncertainties $\Delta_{res}/\Delta_{min}$ with increasing $\sigma_\chi/\sigma_{noise}$ for a higher projected rotational velocity, $v \sin(i) = 145 \text{ km s}^{-1}$. Uncertainty and line definitions are the same as in Figure 5.

For the second test, we again use an artificial spectrum (with the following parameters: $T_{eff} = 21350 \text{ K}$, $\log(g) = 3.80$, $v \sin(i) = 125 \text{ km s}^{-1}$, $\xi = 3 \text{ km s}^{-1}$, and solar chemical composition) but this time we change the noise level added to it in order to create different signal-to-noise ratios (SNR), ranging from 25 to 350 per resolution element with a step of 25. We estimate the SNR using the *der_snr* program of Stoehr et al. (2008). On this scale, a SNR of 250 corresponds to a σ_{noise} of approximately 0.004 in the normalized continuum. For each value of SNR, we create 10 noisy artificial spectra. For the 140 new spectra thus created, we apply our method with the original definition of σ_χ (Eq. 7). This way we simulate a real analysis even though we still are in the case of a perfect model and imperfect data. Of course, in this case σ_χ is overestimated by roughly a factor of 2, since for a given line k , $(\sigma_{model})_k \approx \sigma_{noise}$, but as explained above, it has nearly no incidence on the method accuracy. The final parameters returned by the 140 runs are shown in Figure 7 and the overall success rate of the method is shown in Figure 8. This test allow us to check for the robustness of the method against highly noisy data, and we can see that for SNR around 100-125 and higher, the method returns correct and accurate results (with uncertainties equal or close to the minimal uncertainties and with a mean success rate of 97.5%). For lower SNR (≤ 100), the parameter uncertainties become naturally larger but the real parameter values are still found nearly 84% of the time (within the uncertainties). Considering all the SNR values, the overall success rate is around 94%.

The third test is the same as the second one, except that the artificial spectrum is created with the atmospheric model ATLAS9 (Castelli & Kurucz 2004), rather than with TLUSTY, using the same stellar parameters. This test is close to an analysis of real data since we are in the case of imperfect data and inexact models. The results are shown in Figure 9, and the overall success rate of the method in Figure 10. Compared to Figure 7, we can see from Figure 9 that the best parameters returned by the method for the spectrum without noise (orange lines) are different than the real parameters (green lines) used to create the spectrum. It is especially true for the effective temperature (the other parameters are within the minimal uncertainties), where $T_{effBest} = 21930 \text{ K}$ while $T_{effReal} = 21350 \text{ K}$. This discrepancy is to be expected when comparing full non-LTE (i.e. non-LTE atmospheric models with non-LTE radiative

transfert) spectra with hybrid LTE/non-LTE (i.e. LTE atmospheric models with non-LTE radiative transfert) spectra since, non-LTE line profiles tend to be slightly stronger and broader than those derived from LTE atmospheres, thus giving a lower temperature when considering a LTE treatment (Huang, Gies & McSwain 2010; Lanz & Hubeny 2007). Here the artificial spectrum is created by a hybrid model while the grid of synthetic spectra are calculated using a full non-LTE treatment. Therefore our method finds a higher effective temperature than the one used to create the hybrid spectrum. Note that this discrepancy is not taken into account by σ_{model} since this parameter reflects the model incapacity to correctly reproduce the lines (whatever parameter values are considered). Here, our model is able to reproduce nearly perfectly most of the lines but for a different effective temperature than the one used to create the hybrid lines. With this in mind, if we consider the best parameter values found for the hybrid spectrum without noise as the reference values (rather than the real values used to create the hybrid spectrum), we find a mean success rate of nearly 93% (Fig. 10) which is equivalent to the success rate found in the previous test (Fig. 8). Note that if we consider the original parameter values, the mean success rate for all the parameters is around 75%, and around 96% when we exclude T_{eff} . In tests 2 and 3, if we multiply the derived parameter uncertainties by a factor 1.5 or 2, the overall success rate (which is around 94% in both case) jumps to nearly 98% and 99%, respectively. Thus, in terms of classical statistics, our results are given with an accuracy close to a 2σ uncertainty.

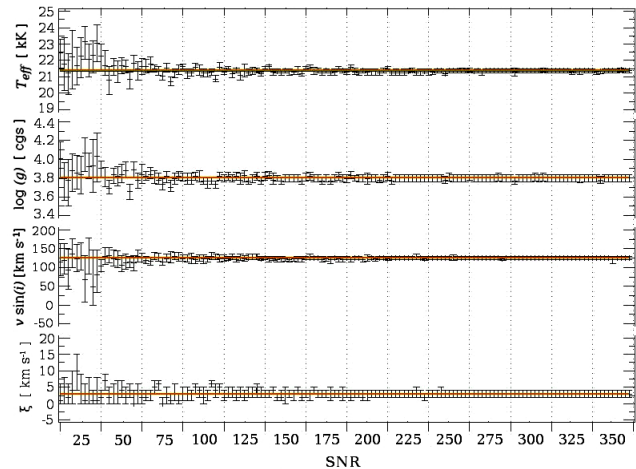


Figure 7. Plot of the stellar parameter values as a function of the signal-to-noise ratio. For each SNR value, 10 artificial spectra with a random noise structure are tested. The green lines show the real parameter values used to create the original artificial spectrum ($T_{eff} = 21350$ K, $\log(g) = 3.80$, $v \sin(i) = 125$ km s⁻¹, and $\xi = 3$ km s⁻¹). The orange lines show the best parameters returned for the artificial spectrum without noise added. The orange lines often overlap with the green lines.

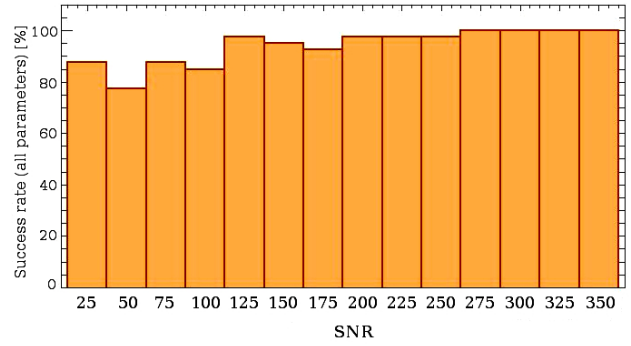


Figure 8. Success rate of the method, to derive the correct parameter values (within the uncertainties) used to create the original artificial spectrum, as a function of the signal-to-noise ratio. Percentages are mean values gathered from all the parameters for each SNR value.

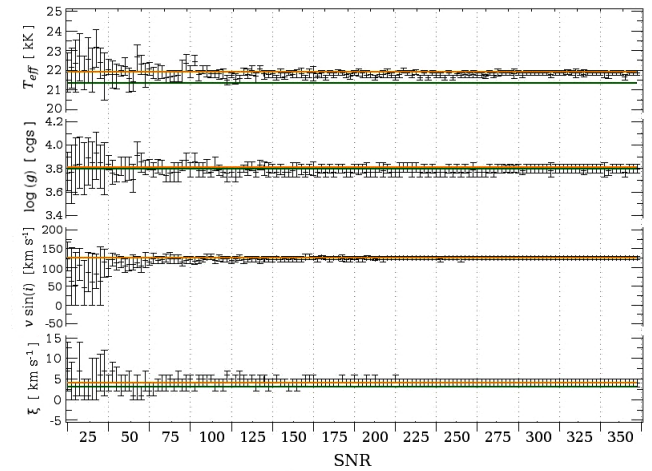


Figure 9. Same test as in Figure 7 when using an artificial spectrum created by the atmospheric model ATLAS9. The green lines show the real parameter values used to create the original artificial spectrum ($T_{eff} = 21350$ K, $\log(g) = 3.80$, $v \sin(i) = 125$ km s⁻¹, and $\xi = 3$ km s⁻¹). The orange lines show the best parameters returned for the original spectrum without noise added ($T_{eff} = 21930$ K, $\log(g) = 3.81$, $v \sin(i) = 125$ km s⁻¹, and $\xi = 4$ km s⁻¹). The orange line overlaps the green line in the case of $v \sin(i)$.

4 TESTING OUR METHOD ON REAL STELLAR SPECTRA

4.1 Observational Data

The selection criteria for our sample were as follow: 1) only mid-B to early-B type stars, since the pre-calculated *BSTAR2006* atmospheric models only cover the range of effective temperature for these subtypes; 2) relatively bright stars to allow a high SNR; 3) no binaries or peculiar stars to avoid complications while testing our method; 4) relatively close objects in order to work with a solar chemical abundance approximation (chemical element abundances will be the topic of a following paper); and 5) well known objects to allow the comparison of our method with other works. The main studies used here for the comparison are from Huang, Gies & McSwain (2010, hereafter HG10), Lefever

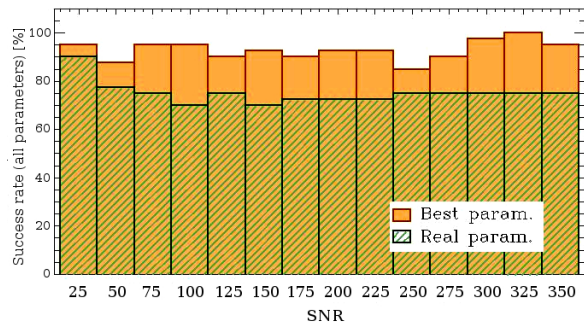


Figure 10. Success rate of the method, to derive the correct parameter values (within the uncertainties), as a function of the signal-to-noise ratio. Here the correct parameter values are either the values used to create the hybrid artificial spectrum (*Real param.*), or the best values found when analysing the artificial spectrum without noise (*Best param.*). Percentages are mean values gathered from all the parameters for each SNR value.

et al. (2010), Takeda et al. (2010), Searle et al. (2008), Markova & Puls (2008), Daflon et al. (2007), Huang & Gies (2006a,b, hereafter HG06), Lyubimkov et al. (2005), and Andrievsky et al. (1999).

We test our method on a sample of 54 mid-B to early-B stars, where 38 are from the field and 16 from clusters. The field stars are all nearby dwarf and giant B stars, with a visible magnitude $3.8 \leq V \leq 9.7$. The cluster stars are members of two open clusters: 8 B stars from NGC1960 (M36) with $8.8 \leq V \leq 10.8$, and 8 B stars from NGC884 (χ Persei) with $8.9 \leq V \leq 11.6$. These two clusters have a colour excess $E(B - V) = 0.22$ and 0.56 , respectively, and due to their proximity, are assumed to have a metallicity close to solar (Kharchenko et al. 2005). The spectra have been collected at the 1.6 m telescope of the Observatoire du Mont-Mégantic at 3 epochs: February 2011, August 2013, and December 2013. They cover the wavelength range from 3500 to 5500 Å with a spectral resolution of 2.3 Å and a mean SNR of 250 per pixel in the continuum (with very little variation from the blue to the red end). We select all the observed lines available for the spectral analysis, except when they are not reproduced by the models, when they are barely distinct from the noise, or when they are superimposed on bad CCD pixels. Table 1 lists all the major useful lines. Note that not all these lines are available for every stars since they may appear or disappear depending on the spectral type. Note also that due to our modest resolution, and sometimes due to strong rotational velocities, more minor lines are included in the analysis.

4.2 Results and Discussions

We apply our method using most of the available lines for all 54 spectra. Figures 11 and 12 show 4 examples of the best fits obtained with a small and a high rms, respectively. All the other quality fits are between these extreme examples. For all stars, the fit is globally good when considering the whole spectrum while it may vary from excellent to decent when considering each line individually. For instance, HD215191 in Figure 11 has a global rms of 0.0038, while individual lines have a rms between 0.0011 and 0.0085. This is because the method returns the best solution for all the lines at

Table 1. Principal spectral lines used for the analysis

Species	Wavelength (Å)
H I	3712, 3722, 3734, 3750, 3771, 3798, 3835, 3889, 3970, 4102, 4340, 4861
He I	3785, 3820, 3867, 3872, 3927, 3936, 4009, 4026, 4121, 4144, 4169, 4388, 4438, 4471, 4713, 4922, 5016, 5048
C II	4267, 4374, 4619, 4619, 5133, 5145, 5648
N II	3995, 4044, 4228, 4237, 4447, 4601, 4607, 4631, 4803, 4994, 5667, 5680
O II	3912, 3954, 3982, 4070, 4079, 4085, 4153, 4185, 4277, 4304, 4317, 4320, 4367, 4415, 4501, 4591, 4642, 4649, 4662, 4676, 4705, 4907, 4943
Mg II	4481
Al III	4513, 4529, 5697
Si II	3856, 3863, 4131, 5056
Si III	4553, 4568, 4575, 4683, 4829, 5740
Si IV	4089
S II	4294, 4525, 4816, 5032, 5103, 5321, 5433, 5454
S III	4254, 4285, 4362
Fe II	5169, 5260
Fe III	5074, 5087

the same time *and not the best solution for each line taken individually.*

Concerning NGC1960 SAB30 (Fig. 12 upper panel), the poor quality of the fit (by far the worse case in our sample) is mainly due to the fact that this star has an effective temperature beyond the reach of our model. Its effective temperature is most likely around 13000 K (HG06), while our grid can only go down to 15000 K. This is also the case for NGC1960 SAB23 (Fig. 12 second panel) but to a lesser extent, since its effective temperature seems to be closer to 15000 K (HG06) than for SAB30.

For HD40160 (Fig. 12 lower panel), we encountered some difficulty during the reduction process, due to the presence of humidity spots on the CCD at the time of the observation, making the $H\beta$ line unusable, altering the shape of $H\gamma$ (i.e. a shallower centroid), and reducing the number of usable lines in general. We still performed the analysis of this star as an extreme test for the sensitivity of our method to the number and quality of the lines used. While our results for HD40160 are not extremely different from those found in the literature, they present one of the largest discrepancy of our results with other works, and therefore are not considered in the remaining of this paper. In particular, we find $T_{eff} = 20010_{-240}^{+290}$ K, $\log(g) = 4.05_{-0.05}^{+0.07}$, $v \sin(i) = 128_{-8}^{+7}$ km s⁻¹, and $\xi = 5_{-2}^{+1}$ km s⁻¹, while HG06 found $T_{eff} = 16453 \pm 250$ K, $\log(g) = 3.735 \pm 0.027$, $v \sin(i) = 115 \pm 35$ km s⁻¹, and $\xi = 2$ km s⁻¹.

Figure 13 compares our results with those from other groups. All the numerical values can be found in Tables B1 (for field stars) and Table B2 (for cluster stars), where the

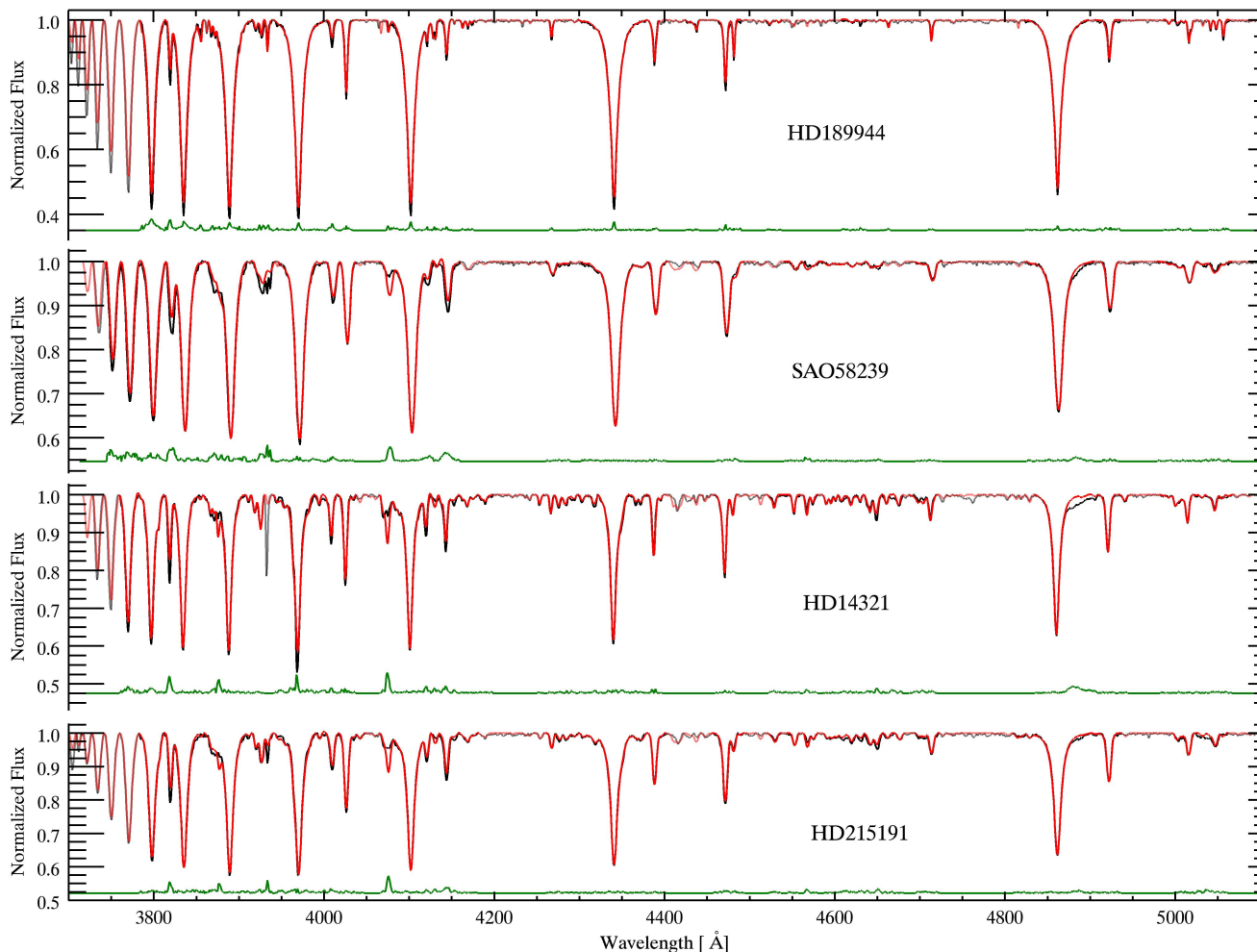


Figure 11. Examples of the best fits obtained for four B stars in our sample. These fits have the smallest averaged rms of our sample (from top to bottom, the averaged rms are 0.0043, 0.0042, 0.0041, and 0.0038). Observed spectra are in black, best synthetic spectra are in red, and the offset rms are in green. Regions of spectra not used for the analysis are in lighter colour.

uncertainties given by our method (as explained in §2.2) are generally smaller than those found in the literature, because of the cumulative effect of our method (as explained in Fig. 2). While most of the time there is a good agreement between our results and those from other works, there are some important discrepancies. These are discussed in the following subsections.

4.2.1 Chemical Abundances

In this paper we want to do a study of the impact of the spectral synthesis method used on the stellar parameters, therefore it is important that we first demonstrate that the discrepancies in Figure 13 are not associated to the chemical abundances considered by the different analysis. Some of the other works used here for comparison derived the abundances of a few chemical elements at the same time that they determined the basic stellar parameters, while we are considering a solar abundance, based on Asplund et al. (2009), as the standard chemical composition for the models for all the stars in our sample. Nevertheless, the variations of the abundances found by the other authors are small, the overall metallicity is solar, and this distinction is

not the main reason for the discrepancies found in Figure 13. To demonstrate this, we repeat the analysis of the stars in our sample using the abundances derived by the other works. Specifically, we adopt the abundances of the following chemical elements: He and Si from LEF10 (Table B3); O and Ne from TAK10 (Table B4); C, N and O from SEA08 (Table B5); He and Si from MAR08 (Table B6); C, N, O, Mg, Al, and Si for DAF07 (Table B7); He and Mg from LYU05 (Table B8); and C and N from AND99 (Table B9), for the stars that we have in common. HG10 and HG06 did not derive the abundances for any specific elements but they used the atmospheric model ATLAS9 with the solar abundances from Grevesse & Sauval (1998), as we also redo for the corresponding stars (Tables B10 and B11). Note that HG10 and HG06 derived T_{eff} and $\log(g)$ using ATLAS9, but determined $v \sin(i)$ using TLUSTY models and as such, one should consider only Figure 13 for a proper comparison of $v \sin(i)$. Figure 14 shows the comparison of our new results, with the other papers, obtained when we are using their abundance data. When comparing Figures 13 and 14, we see a small and marginal difference between the two set of results (except for the stars studied by HG10 which we discuss in more details in §4.2.2. We believe that the reason

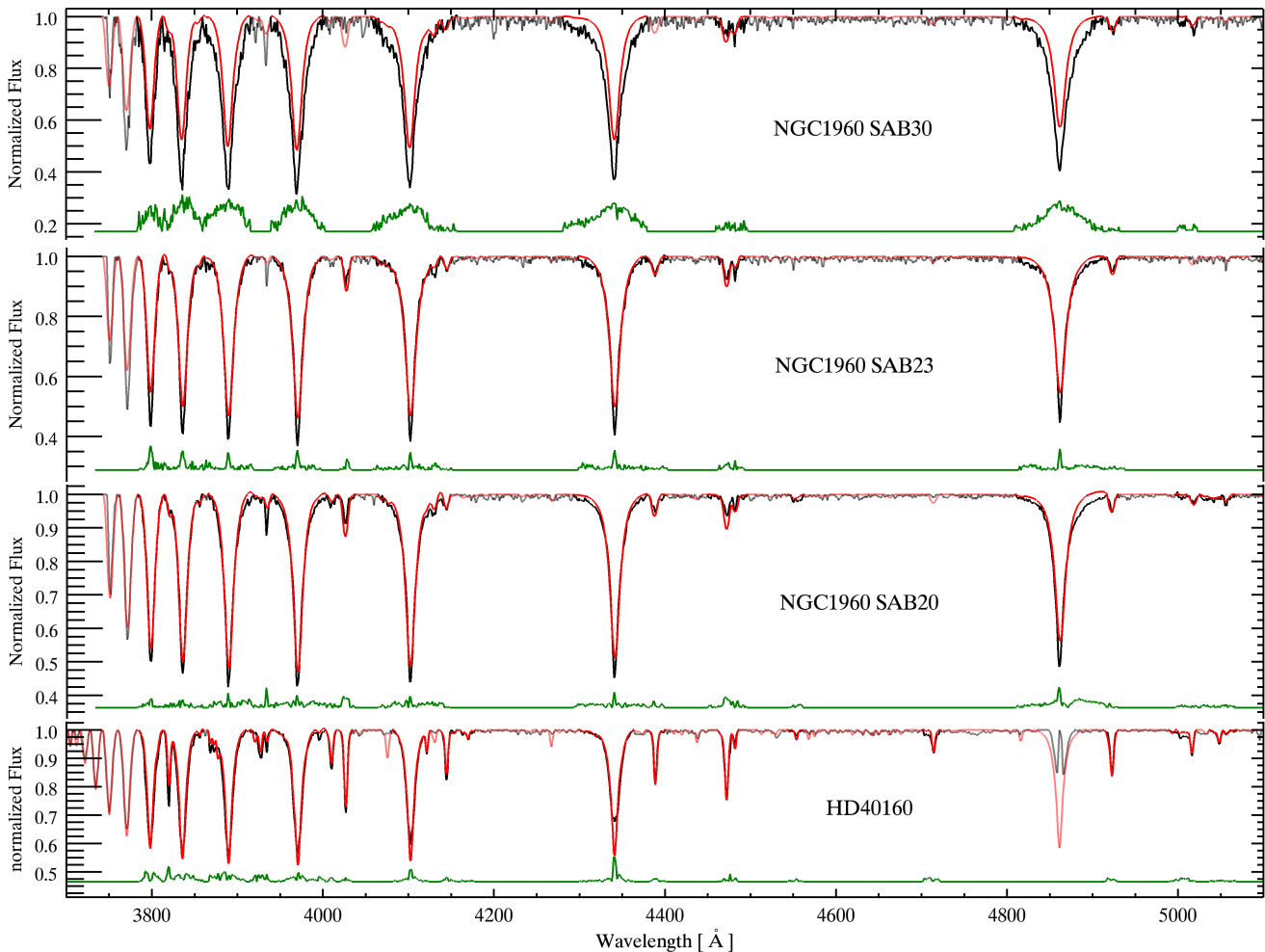


Figure 12. Examples of the worst fits obtained for four B stars in our sample. These fits have the highest averaged rms of our sample (from top to bottom, the averaged rms are 0.05, 0.011, 0.0098, and 0.0088). Colours are as in Figure 11.

for the small change between the two figures is mainly related to the fact that the element abundances derived by the other authors were tailored to a few lines only and have little impact on the other parameters obtained simultaneously by fitting the whole spectrum as is done with our method. As discussed in the following subsections, we find that the impact of the method used and the choice of the diagnostic lines is more important to explain the discrepancies seen in Figures 13 or 14. A complete analysis with our method, including abundances determination and their effect on the basic stellar parameters, will be done in a following paper.

4.2.2 Effective Temperature and Surface Gravity

Figure 13, or 14, often shows a large scattering for the effective temperature and the surface gravity. Among others, we see a quasi-systematic difference between our estimates of T_{eff} and $\log(g)$ and those of HG10 and HG06. We believe that the main reason for this is related to the fact that these authors used only $H\gamma$ as a diagnostic line. For the 30 stars that we have in common with HG10 and HG06, we perform our analysis using the atmospheric model ATLAS9 and the solar chemical composition of Grevesse & Sauval

(1998) with all the available spectral lines (these results are presented in Fig. 14), but also, with only $H\gamma$ as a diagnostic line. Figure 15 shows for the 30 stars the effect on T_{eff} and $\log(g)$ of the number of diagnostic lines used, as well as the effect of the different models. From the upper panels of Figure 15, we see that a change of atmospheric model or chemical composition (TLUSTY with the solar composition of Asplund et al. 2009 in red versus ATLAS9 and the solar composition of Grevesse & Sauval 1998 in green) has little impact on the discrepancies between our results and those of HG10 and HG06: the discrepancies remain important. Whereas the lower panels shows that considering only $H\gamma$ as a diagnostic line drastically reduces the variations in T_{eff} , and greatly affect those in $\log(g)$. For instance, the 3 stars in Figure 13 with a large difference in T_{eff} , when compared to HG10, are the most extreme examples of this effect (they are the stars number 23, 24, and 25 in Figure 15). It is clear in this case that the number and choice of diagnostic lines used has a greater impact on the determination of T_{eff} and $\log(g)$ than the choice of the atmospheric model or the solar chemical composition.

Furthermore, the choice of the diagnostic line, when only one is used, also affects the results. Figure 16 shows the best values of T_{eff} and $\log(g)$ that we obtain for differ-

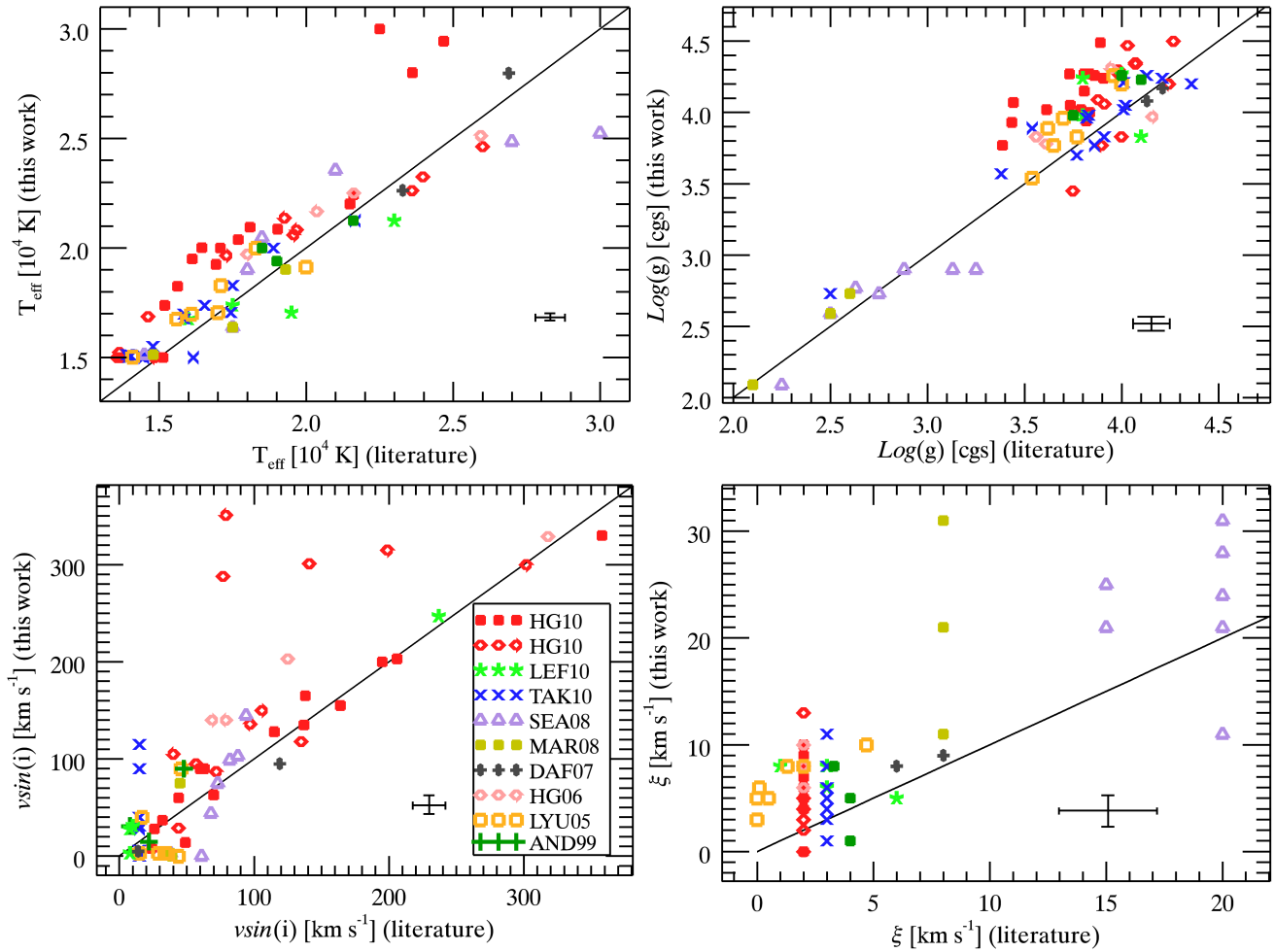


Figure 13. Comparison of our results for T_{eff} , $\log(g)$, $v \sin(i)$, and ξ with other works from the literature. Atmospheric models from TLUSTY with the solar composition from Asplund et al (1999) have been used. Open diamonds are cluster stars and the other symbols are field stars. Mean error bars for these data are shown in black. The black full line indicates a one-to-one match. Note that some of our stars have been studied in more than one paper and thus appear multiple times in the graphics. The abbreviations in the legend correspond to the following papers: HG10 for Huang, Gies & McSwain (2010); LEF10 Lefever et al. (2010); TAK10 Takeda et al. (2010); SEA08 Searle et al. (2008); MAR08 Markova & Puls (2008); DAF07 Daflon et al. (2007); HG06 Huang & Gies (2006a,b); LYU05 Lyubimkov et al. (2005); and AND99 for Andrievsky et al. (1999).

ent values of $v \sin(i)$ when only H β , H γ , or H δ is considered for the analysis. This analysis is done using an artificial spectra with $T_{eff} = 21350$ K, $\log(g) = 3.8$, $\xi = 3$ km s $^{-1}$, and $v \sin(i) = 15$ km s $^{-1}$. In Figure 16, we can see that each line has a different sensitivity over $v \sin(i)$ and that two lines rarely give the same results for a given $v \sin(i)$. Moreover, T_{eff} and $\log(g)$ given by H γ are lower than the real values by 2350 K and 0.3 dex, respectively, when $v \sin(i)$ is close to its real value. These differences are of the order of the quasi-systematic difference seen between HG10, HG06, and our work.

When comparing our results for the evolved stars with those obtained by Searle et al. (2008) in Figure 13, we find similar temperatures for the stars below 20000 K, and less scatter than Searle et al. (2008) for the stars above (the effective temperature goes from 23500 K to roughly 25000 K in our work, while the authors found temperatures going from 21000 K to 30000 K). The $\log(g)$ values are, within the uncertainties, quite identical, with $\log(g)$ below 3 in our case.

We also find higher microturbulence velocities and a larger scatter for the rotational velocity. Note that performing our analysis with the C, N, and O abundances derived by Searle et al. (2008) has little to no impact on the observed discrepancies (as shown when comparing Figures 13 and 14). The reason for the differences between our results and those of Searle et al. (2008) may be related to two important effects:

- 1) First of all, Searle et al. (2008) used a combination of TLUSTY and CMFGEN in order to include wind effects which we are not doing. For instance, in B supergiant, the Balmer lines could suffer from wind contamination, where photons emitted by hydrogen atoms in the wind “fill in” the absorption profiles thus making them shallower than any profiles calculated with a photospheric model (Searle et al. 2008). It is especially true for H α and H β and to a lesser extent for H γ and the other Balmer lines. Other photospheric lines can also be influenced by winds, such as the Si IV $\lambda 4089$ line and the Si III $\lambda \lambda 4552, 4568, 4575$ multiplet (Hillier et al. 2003; Dufton et al. 2005; Searle et al. 2008). But since this

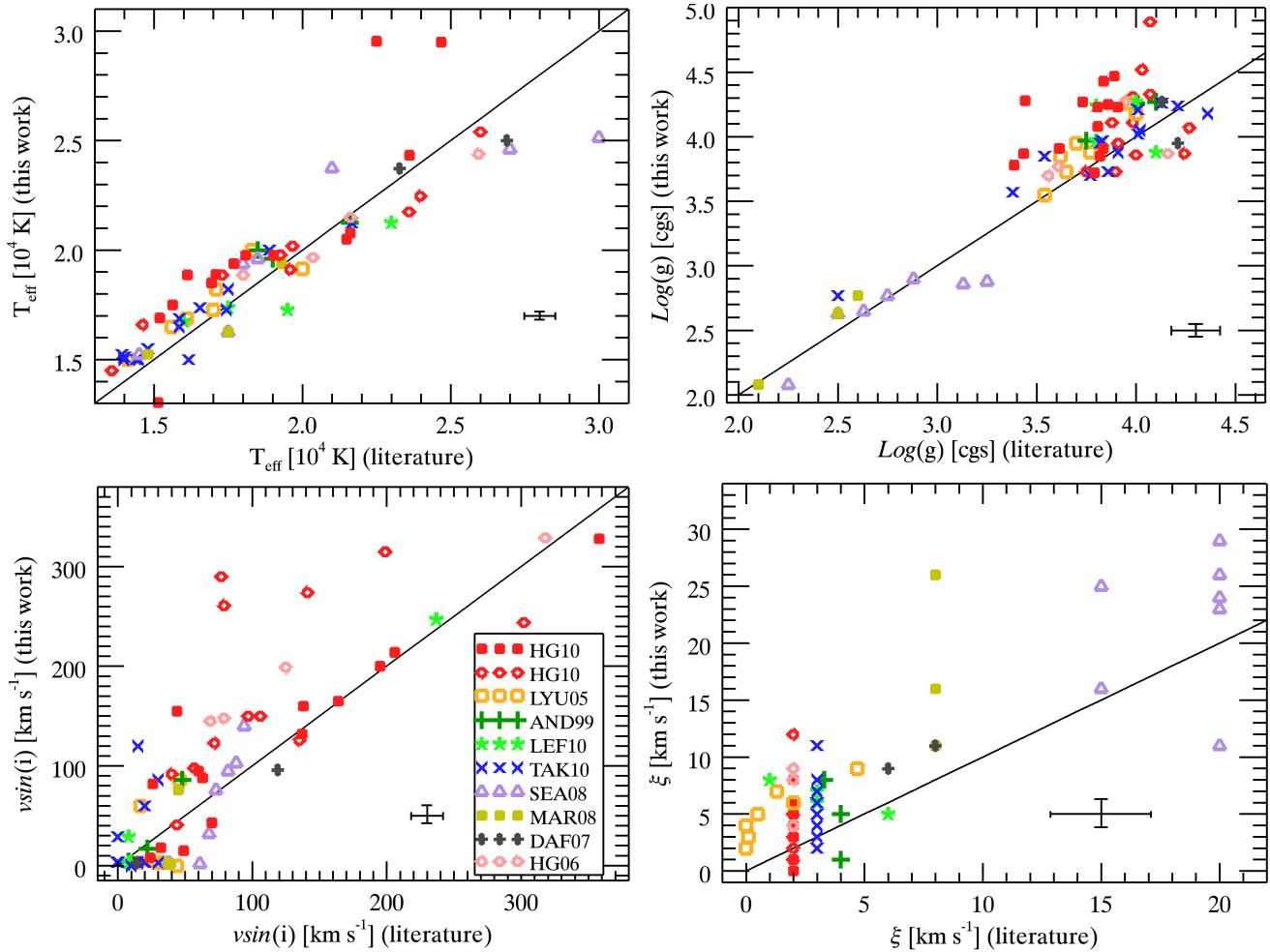


Figure 14. Comparison as in Figure 13 but with the individual chemical abundances fixed, in our analysis, to the values given by other papers. The modified chemical elements are as follow: He and Si for a comparison with LEF10; O and Ne for TAK10; C, N, and O for SEA08; He and Si for MAR08; C, N, O, Mg, Al, and Si for DAF07; He and Mg for LYU05; and C and N for a comparison with AND99. No individual chemical abundance modifications were considered for the stars in common with HG10 and HG06, but we used the atmospheric model ATLAS9 with the solar abundances of Grevesse & Sauval (1998) in this case. Note that we find some stars with $T_{\text{eff}} < 15000$ K since the grid calculated with ATLAS9 has a broader range in T_{eff} than our grid created with TLUSTY. Also, while HG10 derived T_{eff} and $\log(g)$ using ATLAS9, these authors used TLUSTY to derive $v \sin(i)$, the comparison for this parameter is thus irrelevant here.

influence seems to be model dependant, it is therefore difficult to correctly quantify it. Nevertheless, it is not really surprising that among the 8 program stars that we have in common with Searle et al. (2008), the 3 stars that exhibit the strongest differences in T_{eff} and $\log(g)$ are the ones with the strongest mass-loss rate (according to Searle et al. 2008 measurements). These 3 stars are HD192660, HD213087, and HD190066. Respectively, their mass-loss rates are 5, 0.7, and $0.7 \times 10^{-6} M_{\odot} \text{ yr}^{-1}$, their effective temperature differences are 4290, 3250, and 2370 K, and their $\log(g)$ differences are 0.3, 0.27, and 0.07 dex.

2) Furthermore, Searle et al. (2008) used, in an iterative way, different diagnostic lines for different parameters each time, while fixing the other parameters and adopting a rotational velocity found in the literature. While vastly used, due to its simplicity and swiftness, this iterative method may provide a local maximum in the probability space rather than a global maximum because it considers each parameter inde-

pendently. For instance, Searle et al. (2008) used Si IV $\lambda 4089$ and Si III $\lambda \lambda 4552, 4568, 4575$ as primary diagnostic lines for the effective temperature with fixed values of $v \sin(i)$ and ξ . Then they used the effective temperature obtained and the H γ line to determine $\log(g)$. And finally they adopted their pair $[T_{\text{eff}}, \log(g)]$, and a value of $v \sin(i)$ found in the literature, to determine a new microturbulence velocity using the Si III $\lambda \lambda 4552, 4568, 4575$ lines. The whole process was repeated until small changes in the parameters were seen. With this iterative method, the effective temperature returned by the silicon lines greatly depends on the values used for the microturbulence and rotational velocities. And $\log(g)$ obtained from H γ also depends on the effective temperature. Finally, the microturbulence is significantly affected by T_{eff} and $\log(g)$. To illustrate the impact of an iterative method, we create another artificial stellar spectrum with the following specifications: $T_{\text{eff}} = 25000$ K, $\log(g) = 2.8$, $v \sin(i) = 100 \text{ km s}^{-1}$, and $\xi = 14 \text{ km s}^{-1}$.

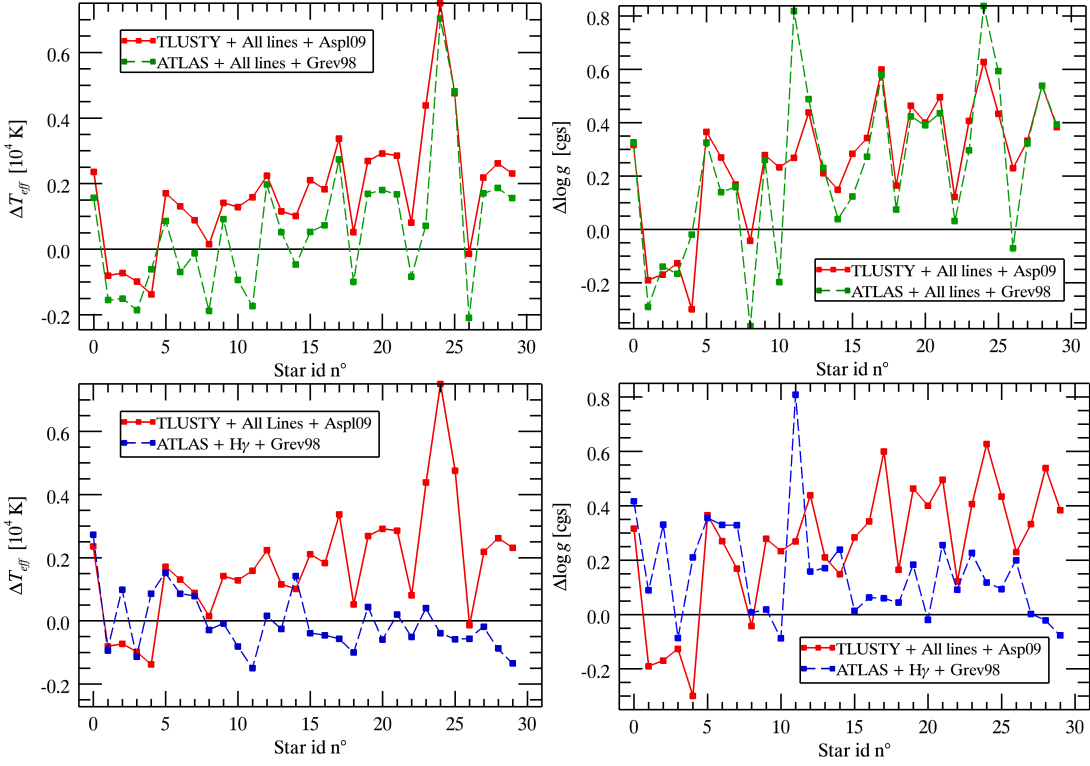


Figure 15. T_{eff} and $\log(g)$ variations for different models and different number of lines for the 30 stars in common with the sample of Huang, Gies & McSwain (2010) and Huang & Gies (2006a). The variations are defined as $\Delta T_{eff} = T_{eff}(this\ work) - T_{eff}(Huang\ et\ al.)$ and $\Delta \log(g) = \log(g)(this\ work) - \log(g)(Huang\ et\ al.)$. *Upper panels:* Variations when considering all the lines but different atmospheric models and solar chemical composition. *Lower panels:* Variations when considering all the available lines or only $H\gamma$.

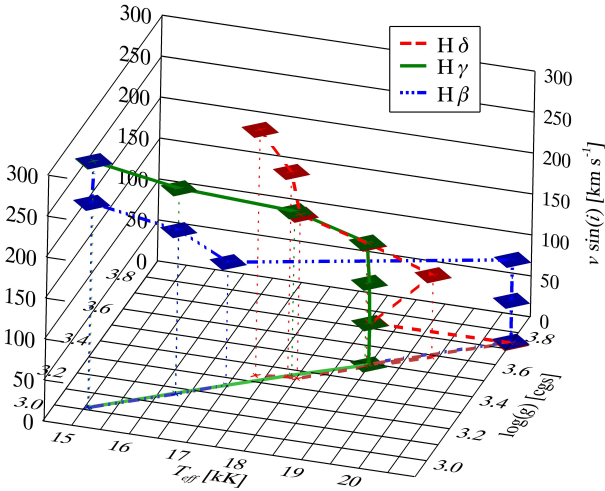


Figure 16. The most probable pair $[T_{eff}, \log(g)]$ as a function of $v \sin(i)$ for different lines (as indicated in the plot) for the artificial spectrum. The parameters used to create the artificial spectrum are: $T_{eff} = 21350$ K, $\log(g) = 3.8$, $\xi = 3$ km s⁻¹, and $v \sin(i) = 15$ km s⁻¹. The behaviour as a function of $v \sin(i)$ is shown projected in the plane $[T_{eff}, \log(g)]$. The likelihoods are marginalized over all ξ values. Note in particular the most probable pair $[T_{eff} 19000$ K, $\log(g) = 3.5]$ given by $H\gamma$ when $v \sin(i) \leq 150$ km s⁻¹.

We then calculate the posterior probability for the 4 silicon lines from this artificial spectrum with the *BSTART* grid. After the marginalization over the $\log(g)$ domain, we find the most probable effective temperature for each given value of ξ and $v \sin(i)$ (Fig. 17, left panel). We then perform the same operation for $H\gamma$ and marginalize over $v \sin(i)$ and ξ (since both parameters have little influence on the returned $\log(g)$ value, showing the marginalized probability is enough in this case) to obtain the most probable $\log(g)$ estimate given each value of T_{eff} (Fig. 17, middle panel). And finally we redo the same analysis, but this time for only the 3 lines Si III $\lambda\lambda 4552, 4568, 4575$ and with a marginalization over $v \sin(i)$ in order to find the most probable value of ξ for each value of T_{eff} and $\log(g)$ (Fig. 17, right panel). To conclude, we can see that the chosen silicon lines almost always overestimate the effective temperature (except when $\xi = 10$ km s⁻¹ and $v \sin(i) \geq 200$ km s⁻¹). Figure 17 also shows a clear anti-correlation: the effective temperature decreases as the rotational velocity increases. Thus if we were to underestimate (respectively overestimate) $v \sin(i)$, we would overestimate (respectively underestimate) T_{eff} . As $\log(g)$ increases with the effective temperature, we would therefore overestimate (respectively underestimate) $\log(g)$. Finally, we would overestimate or underestimate the microturbulence velocity depending on how we estimate $\log(g)$. This behaviour is what we observe between our results and those of Searle et al. (2008) for the stars hotter than 18000 K. For the cooler stars, Searle et al. (2008) used Si III $\lambda\lambda 4128, 4130$ rather than Si IV $\lambda 4089$, which seems to

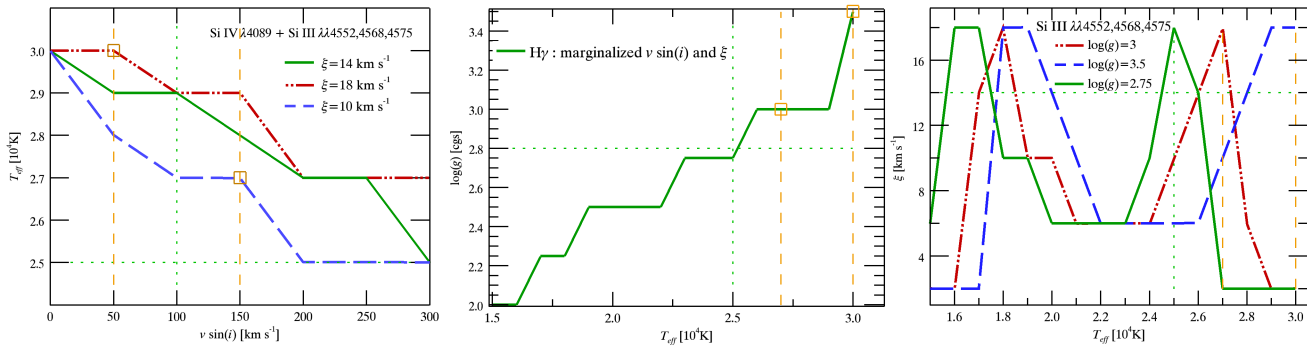


Figure 17. Illustration of the interdependency between T_{eff} , $\log(g)$, and ξ when individual diagnostic lines are considered in an iterative method. The parameters of the artificial spectrum used in this example are: $T_{eff} = 25000$ K, $\log(g) = 2.8$, $v \sin(i) = 100$ km s $^{-1}$, and $\xi = 14$ km s $^{-1}$. *Left Panel:* Most probable effective temperature as a function of $v \sin(i)$ for 3 different microturbulence velocities using Si IV $\lambda 4089$ and Si III $\lambda \lambda 4552, 4568, 4575$. Orange squares and thin orange dashed lines indicate the extreme solutions found when underestimating and overestimating $v \sin(i)$ compared to the parameters used to create the artificial spectrum (thin green dotted lines in all panels). *Middle panel:* Most probable $\log(g)$ values as a function of T_{eff} , after marginalizing over $v \sin(i)$ and ξ while using H γ . Orange squares and orange dashed lines indicate the solution found when overestimating and underestimating T_{eff} from the left panel. *Right Panel:* Most probable microturbulence velocities as a function of T_{eff} , after marginalizing over $v \sin(i)$, for 3 different $\log(g)$ estimates. The full green, dashed blue, and dot-dashed red lines represent the possible values of $\log(g)$ found in the middle panel when overestimating and underestimating T_{eff} . The thin orange dashed lines indicate overestimated and underestimated T_{eff} from the left panel.

induce a smaller effective temperature discrepancy with our method.

Results from the other authors in our comparison list are in a reasonably good agreement with our results even though a wide variety of technics and methods were used. Takeda et al. (2010), Lyubimkov et al. (2005), and Andrievsky et al. (1999) used the *uvby* γ photometric system to derive T_{eff} and $\log(g)$. Our results are quite consistent with theirs. Daflon et al. (2007) derived T_{eff} using the *UVB* photometric system and obtained $\log(g)$ by adjusting the observed H γ line wings with models from ATLAS9. Note that we do not observe the same discrepancies in $\log(g)$ with Daflon et al. (2007), as seen between our results and those of HG10, since on the one hand, Daflon et al. (2007) used T_{eff} values close to ours, and on the other hand, they did not fit the core of the H γ line where non-LTE effects are stronger. Markova & Puls (2008) used a similar approach than Searle et al. (2008): models including stellar wind, $\log(g)$ from Balmer lines, and T_{eff} from Si lines. Our results agree well with theirs since the stars we have in common have weak stellar winds and T_{eff} below or around 18000 K. Finally, Lefever et al. (2010) used a semi-automated iterative method which is close to our simultaneous approach because groups of parameters are derived using a large number of lines simultaneously. Our respective results are in a reasonable agreement considering that Lefever et al. (2010) used models including stellar wind (FASTWIND) and an iterative method.

4.2.3 Projected Rotational Velocity

A substantial difference in Figure 13, between our results and those published in the literature, concerns $v \sin(i)$. The most important discrepancy is found for 4 cluster stars that are also in the sample of HG10 (as mentioned earlier, they also used TLUSTY to derive $v \sin(i)$). We indeed derive higher $v \sin(i)$ values (around 300 km s $^{-1}$) by a factor of

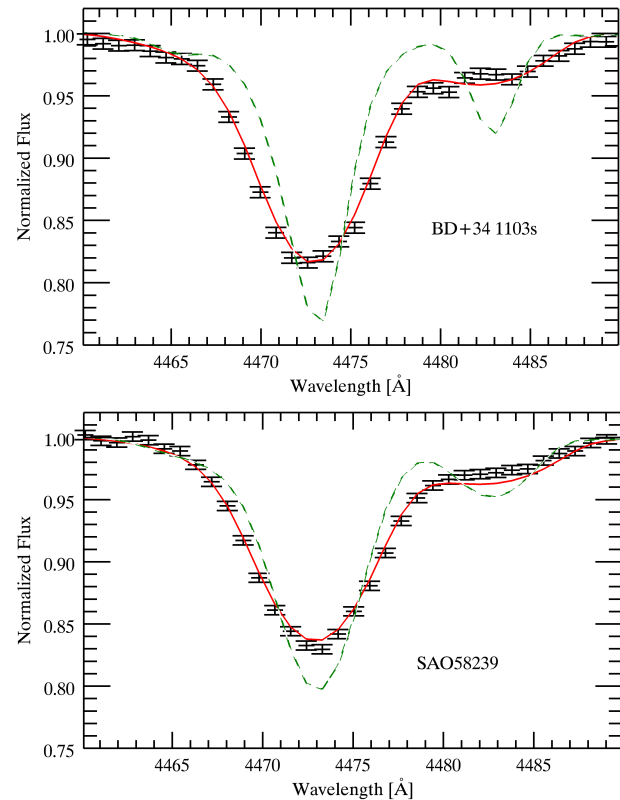


Figure 18. Comparison of the best fits for the lines He I $\lambda 4471$ and Mg II $\lambda 4481$ for 2 stars with large rotational velocities. Individual data points with error bars represent our observations. In full red: models based on our best set of parameters. In dashed green: models using the parameters of HG10. The $v \sin(i)$ values are: 288 km s $^{-1}$ (red) and 77 km s $^{-1}$ (green) for BD+34 1103s; and 315 km s $^{-1}$ (red) and 199 km s $^{-1}$ (green) for SAO58329. The respective complete sets of parameters are listed in Table B2.

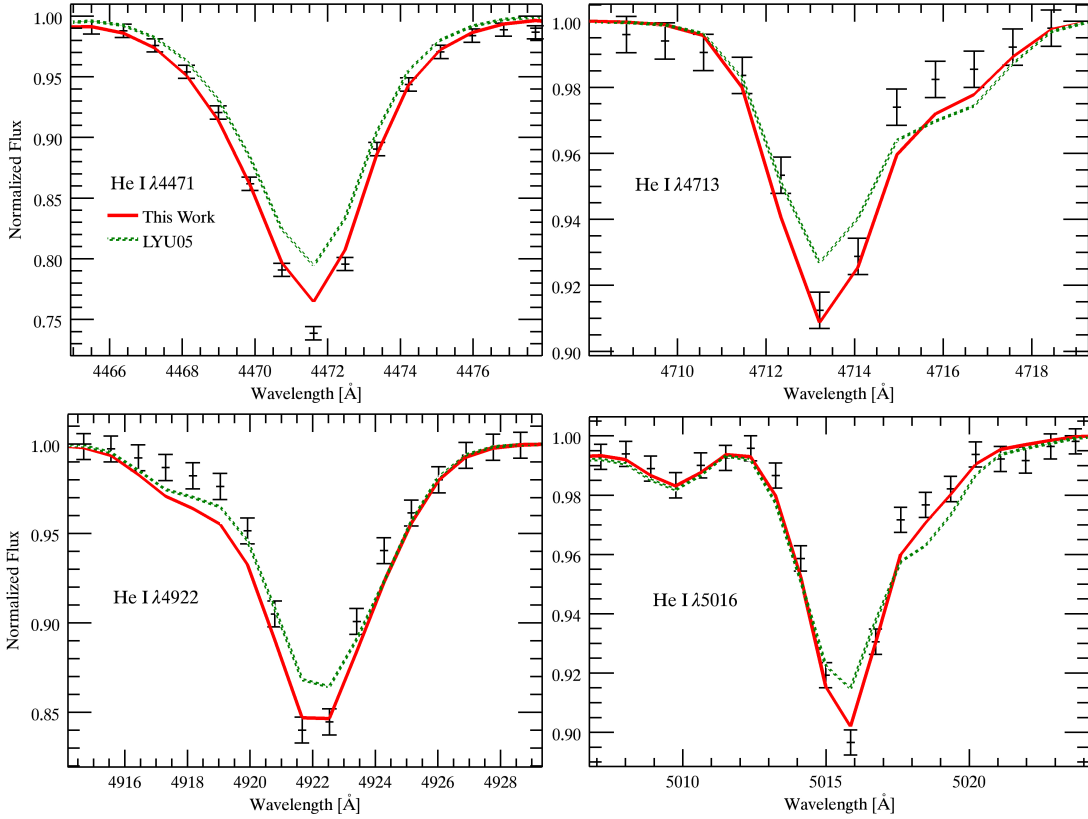


Figure 19. Comparison of the fits for 4 helium lines obtained with our best set of parameters and those from Lyubimkov et al. (2005), for HD184171. Individual data points with error bars represent our observations. In full red: our best model with $T_{eff} = 16890$ K, $\log(g) = 3.89$, $\xi = 3$ km s $^{-1}$, and $v \sin(i) = 3$ km s $^{-1}$. In dotted green: model using the parameters of Lyubimkov et al. (2005): $T_{eff} = 16100$ K, $\log(g) = 3.62$, $\xi = 0$ km s $^{-1}$, and $v \sin(i) = 29$ km s $^{-1}$.

at least 1.5 for BD+34 1103s, NGC1960 SAB20, NGC1960 SAB30, and SAO58239. Of these stars, SAB20 and SAB30 have effective temperatures below our limit of 15000 K and the lowest SNR (around 200 and 75 respectively) objects of our sample. Consequently, the best fits for these stars are among the worst in our sample (Fig. 12) even when using ATLAS9 models, we thus consider that the associated results are not reliable. On the contrary, the other two stars, BD+34 1103s and SAO58239, have excellent SNR and rms (see Fig. 11 for SAO58239). Here, the differences in $v \sin(i)$ cannot be explained simply either in terms of the number or the choice of lines, or in terms of the atmospheric models used, since HG10 also used TLUSTY and SYNSPEC to determine $v \sin(i)$ and we could not reproduce their results using the same lines. One plausible explanation would be the difference in the treatment of $v \sin(i)$ (HG10 used a grid of models based on a three-dimensional parameterization of T_{eff} , $\log(g)$, and the cosine of the angle between the surface normal and the line of sight) but, in this case, there should be a systematic effect between our derived values and theirs for all the cluster stars that we have in common, which we do not observe. Moreover, when we reproduce the lines He I $\lambda 4481$ and Mg II $\lambda 4481$, used by HG10 to derive $v \sin(i)$, we clearly obtain an excellent fit of our own data with our parameters (Fig. 18). We are thus confident of our derived parameters for these two stars even though we have no clear explanation for these discrepancies.

Interestingly, while the differences between our results for $v \sin(i)$ and those of HG10 and HG06 are generally greater for cluster stars than for field stars, and even though our sample is not large, we still find the same conclusion as HG06, i.e. cluster stars are globally faster rotators than field stars. From our results, cluster stars are even faster rotators.

Another issue concerning $v \sin(i)$ in Figure 13, or 14, appears at relatively low rotational velocities ($v \sin(i) \leq 100$ km s $^{-1}$). In this case, there is a rather large scatter between our results and those from other authors. Some of the largest differences can either be explained by our limited range in temperature (for example, Takeda et al. 2010 found $v \sin(i) = 15$ km s $^{-1}$ for HD185330, while we find $v \sin(i) = 115$ km s $^{-1}$ because the effective temperature is most certainly below 15000 K), or by the parameters and spectral lines considered. For instance, the $v \sin(i)$ values of Lyubimkov et al. (2005) are mostly between 15 and 50 km s $^{-1}$, while ours are between 0 and 10 km s $^{-1}$ with an uncertainty around 10 km s $^{-1}$ for the same stars. Lyubimkov et al. (2005) derived their velocities using fixed values of T_{eff} and $\log(g)$, free values of $v \sin(i)$, ξ , and helium abundances, and considered 6 helium lines, while we use solar helium abundance, free values of T_{eff} , $\log(g)$, $v \sin(i)$, and ξ , and more spectral lines. While helium abundance has an obvious impact on the shape of helium lines, relatively small changes in T_{eff} , $\log(g)$, and ξ also have an influence on the resulting $v \sin(i)$ value. For instance, when consid-

ering HD184171 with $T_{eff} = 16100$ K and $\log g = 3.62$, Lyubimkov et al. (2005) found a solar helium abundance, $v \sin(i) = 29$ km s⁻¹, and $\xi = 0$ km s⁻¹, while we obtain $T_{eff} = 16890$ K, $\log g = 3.89$, $v \sin(i) = 3$ km s⁻¹, and $\xi = 3$ km s⁻¹ for a solar helium abundance. Figure 19 shows the models for these 2 sets of parameters for 4 helium lines (that are among the 6 helium lines used by Lyubimkov et al. 2005). From this figure, it is clear that, with our set of parameters, a higher value of $v \sin(i)$ would not improve the fits. Note also that our parameters are derived from the analysis of more than these 4 helium lines (27 in this case), and as such are more constrained, thus explaining the small uncertainties. Indeed, if we perform an analysis using only these 4 helium lines, with T_{eff} , $\log(g)$, and ξ fixed to their best values, the uncertainty for $v \sin(i)$ goes roughly from ± 10 to ± 20 thus reducing the discrepancy between our results and those of Lyubimkov et al. (2005).

There is also an interesting point concerning low rotational velocities and their respective uncertainties. Indeed, HG10 noted that depending on the resolution of a given spectrum, and for $v \sin(i)$ less than half the FWHM of the instrumental broadening function, the instrumental broadening dominates the rotational broadening, implying uncertainties of the order of $\pm \text{FWHM}/2$ for low $v \sin(i)$ values. In the work of HG10, $\text{FWHM} \approx 0.8$ and 1.5 Å resulting in uncertainties of 29 and 48 km s⁻¹, respectively, for $v \sin(i)$ below these values. Our data have a FWHM of 2.3 Å, and thus the theoretical limit is around 80 km s⁻¹. But, as our method cumulates the constraints of a large number of lines, it allows us to significantly reduce this limit. Figure 20 shows, for each star, the maximum uncertainty of $v \sin(i)$ as a function of $v \sin(i)$. Here, we see that the method generally and naturally returns larger uncertainties for $v \sin(i) \leq 80$ km s⁻¹ than for higher values, but with a maximum uncertainty (for low $v \sin(i)$) of roughly 30 km s⁻¹ well below the limit of 80 km s⁻¹. As a further demonstration, we apply our method on higher spectral resolution data of two stars in our sample, obtained with a different grating at the Observatoire du Mont-Mégantic (in February 2011). These two stars are HD77770 and HD44700, whose spectra have an effective resolution of 0.9 Å and a wavelength range spanning from 3600 to 4400 Å. The results for T_{eff} , $\log(g)$, and ξ obtained for these two stars are the same (within the uncertainties) at moderate and high resolution. But for $v \sin(i)$, HD77770 gives 0_{-0}^{+13} km s⁻¹ at high resolution, rather than 14_{-14}^{+6} km s⁻¹ at moderate resolution, and HD44700 gives $v \sin(i) = 4_{-4}^{+10}$ km s⁻¹, at high resolution, rather than 28_{-22}^{+18} km s⁻¹ at moderate resolution.

4.2.4 Microturbulence Velocity

Finally, one of the most obvious difference in Figure 13, or 14, lies with the microturbulence velocity but it is simply explained by the fact that, in most works, the microturbulence velocity is not a free parameter. Usually ξ is fixed at about 3 km s⁻¹ and 10 km s⁻¹ for main-sequence stars and for evolved stars, respectively (HG10; Takeda et al. 2010). And, when the microturbulence velocity is not fixed, it is estimated with only one or two lines in the spectrum (Lyubimkov et al. 2005) or with only one species (Lefever et al.

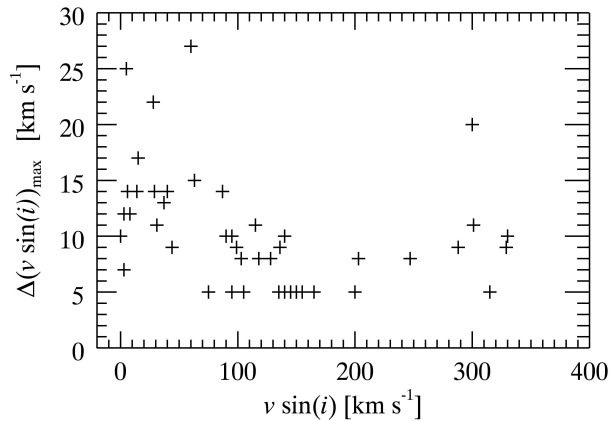


Figure 20. Maximum uncertainty for $v \sin(i)$ as a function of $v \sin(i)$ for our whole sample.

2010). When considering all the available lines to fit the microturbulence velocity simultaneously with the other parameters, we find a higher estimate than what is generally used. We obtain a mean microturbulence velocity of 6.1 km s⁻¹ with a standard deviation of 2.6 km s⁻¹ for the main-sequence stars, and a mean value of 21.4 km s⁻¹ with a standard deviation of 7.6 km s⁻¹ for the evolved stars. Note that our results are given for solar abundances, but even though we find slightly lower values of microturbulence velocity (by nearly 2 km s⁻¹) when we use the abundances derived by the various authors, our values are still higher than those from the literature.

Fixing or constraining the microturbulence velocity with only a few lines can lead to large errors for the other parameter estimates as well. Figure 21 shows an example of the most probable pairs $[T_{eff}, \log(g)]$ for $\xi = 2, 6, 10, 14,$ and 18 km s⁻¹ when calculating the likelihoods with the lines He I $\lambda 4388$, He I+Mg II around 4476 Å, Si II $\lambda \lambda 4128, 4130$, and Si III $\lambda \lambda 4552, 4567, 4574$ of the artificial spectrum with the following specifications: $T_{eff} = 21350$ K, $\log(g) = 3.8$, $\xi = 3$ km s⁻¹, and $v \sin(i) = 15$ km s⁻¹. This shows that each line has a different sensitivity to the microturbulence velocity and, depending on the line or the group of lines chosen as a diagnostic, the result differs in T_{eff} and $\log(g)$ but also in ξ . For instance here, the most probable value of ξ given by the helium lines is 10 km s⁻¹ (when marginalizing over all the other parameters) while the silicon lines give 2 km s⁻¹. Thus, it is very important to consider ξ as a free parameter as is usually done with T_{eff} , $\log(g)$, and $v \sin(i)$, and to constrain these four parameters simultaneously with as many lines as possible. Also it is even more important to consider the microturbulence velocity as a free parameter when studying the abundance, since it has a significant impact on this parameter as well (Nieva & Przybilla 2010).

5 CONCLUSIONS

We described here a spectral analysis method based on Bayesian statistics that simultaneously constrains four stellar parameters (effective temperature, surface gravity, pro-

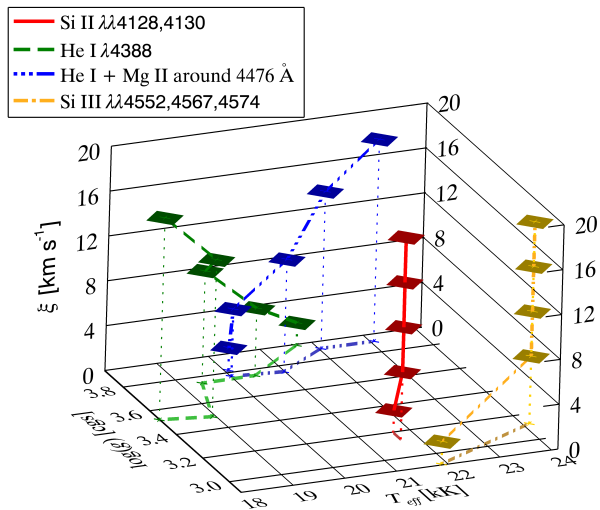


Figure 21. The most probable pair $[T_{eff}, \log(g)]$ as a function of ξ for different lines (as indicated in the plot) for the same artificial spectrum as in Figure 16. The behaviour as a function of ξ is shown in the plane $[T_{eff}, \log(g)]$. The likelihoods are marginalized over all $v \sin(i)$ values.

jected rotational velocity, and microturbulence velocity). The method cumulates the information provided simultaneously by all available lines in a given spectrum. This allows us to find the best global solution for all the lines and all the parameters at the same time, while providing reduced uncertainties. The Bayesian formalism naturally gives the uncertainties for each parameter in relation with the other parameter possible values, with the data uncertainties, and with the limitations of the models used.

This method is completely objective since it does not rely on the user's visual judgement, nor does it depend on starting-parameter estimates. We have shown that adopting an inaccurate starting value or fixing the value of a given parameter, along with using a classical iterative method, can lead to substantial errors on the other parameters. Also, because our method considers all the parameters and all the lines at the same time, it does not depend on the sensitivity of a specific diagnostic line.

This method is also self-consistent and efficient even when it is applied to spectra with high noise level or when underestimating the quality of the data. Moreover, since our method cumulates the constraints of all available lines, it is still able to give accurate results with small uncertainties even though nearly all the lines are heavily blended due to the modest resolution (2.3 \AA) of our data.

Note also, that the method actually works with atmospheric models from TLUSTY but also from ATLAS9 and PHOENIX (Baron, Chen & Hauschildt 2010), and can be easily adapted to virtually any atmospheric model. Furthermore, it is a fast method, once the basic preparation is done (preparation of the data as suitable input for the code and creation of the basic grids) the complete basic parameters analysis of a star takes less than 3 minutes on a typical portable computer (we use a Pentium(R) Dual-Core CPU T4300 @ 2.10GHz with 4 Go of RAM).

Finally, the comparison of our results with those from

the literature is very satisfying overall. Most of the differences found are easily explained in terms of the method used (an iterative method versus our simultaneous method) and the number and choice of the diagnostic lines used (few lines for specific parameters versus, as we did, all available lines with the same weight for all the parameters). One important behaviour is pointed out in this study: the microturbulence velocity is often underestimated for the B dwarfs as well as for the giants and supergiants. Furthermore, we also confirmed that cluster B stars are on average faster rotators than field B stars.

Now that we have demonstrated that we can successfully apply our method to gather stellar parameters using solar abundances, we will investigate in a future paper the impact and efficiency of our method for the abundance determination of various chemical elements.

ACKNOWLEDGMENTS

We thank Ivan Hubeny for generously providing us with the latest version of the SYNPL0T package and for helpful suggestions and comments. We also thank Anthony Moffat and the anonymous referee for a critical reading of the original version of this paper. This work was supported by the Natural Sciences and Engineering Research Council of Canada and by the Fonds Québécois de la Recherche sur la Nature et les Technologies of the Government of Québec.

REFERENCES

- Andrievsky S. M., Korotin S. A., Luck R. E., Kostynchuk L. Y., 1999, *A&A*, 350, 598
- Asplund M., Grevesse N., Sauval A. J., Scott P., 2009, *ARA&A*, 47, 481
- Baron E., Chen B., Hauschildt P. H., 2010, Phoenix: A general-purpose state-of-the-art stellar and planetary atmosphere code. Astrophysics Source Code Library
- Benítez N., 2000, *ApJ*, 536, 571
- Castelli F., Kurucz R. L., 2004, ArXiv Astrophysics e-prints
- Crutcher R. M., Wandelt B., Heiles C., Falgarone E., Troland T. H., 2010, *ApJ*, 725, 466
- Daflon S., Cunha K., de Araújo F. X., Wolff S., Przybilla N., 2007, *AJ*, 134, 1570
- Dufton P. L., Ryans R. S. I., Trundle C., Lennon D. J., Hubeny I., Lanz T., Allende Prieto C., 2005, *A&A*, 434, 1125
- Gregory P., 2010, Bayesian Logical Data Analysis for the Physical Sciences. Cambridge University Press
- Grevesse N., Sauval A. J., 1998, *Space Science Reviews*, 85, 161
- Hillier D. J., Lanz T., Heap S. R., Hubeny I., Smith L. J., Evans C. J., Lennon D. J., Bouret J. C., 2003, *ApJ*, 588, 1039
- Howarth I. D., Siebert K. W., Hussain G. A. J., Prinja R. K., 1997, *VizieR Online Data Catalog*, 728, 40265
- Huang W., Gies D. R., 2006a, *ApJ*, 648, 580
- Huang W., Gies D. R., 2006b, *ApJ*, 648, 591
- Huang W., Gies D. R., McSwain M. V., 2010, *ApJ*, 722, 605

- Kharchenko N. V., Piskunov A. E., Röser S., Schilbach E., Scholz R.-D., 2005, *A&A*, 438, 1163
- Lanz T., Hubeny I., 2007, *ApJS*, 169, 83
- Lefever K., Puls J., Morel T., Aerts C., Decin L., Briquet M., 2010, *A&A*, 515, A74
- Lyubimkov L. S., Rostopchin S. I., Rachkovskaya T. M., Poklad D. B., Lambert D. L., 2005, *MNRAS*, 358, 193
- Markova N., Puls J., 2008, *A&A*, 478, 823
- Mugnes J.-M., Robert C., 2012, in *Astronomical Society of the Pacific Conference Series*, Vol. 465, *Proceedings of a Scientific Meeting in Honor of Anthony F. J. Moffat*, Drissen L., Robert C., St-Louis N., Moffat A. F. J., eds., p. 256
- Nieva M.-F., Przybilla N., 2010, in *Astronomical Society of the Pacific Conference Series*, Vol. 425, *Hot and Cool: Bridging Gaps in Massive Star Evolution*, Leitherer C., Bennett P. D., Morris P. W., Van Loon J. T., eds., p. 146
- Pont F., Eyer L., 2004, *MNRAS*, 351, 487
- Schönrich R., Bergemann M., 2014, *MNRAS*, 443, 698
- Searle S. C., Prinja R. K., Massa D., Ryans R., 2008, *A&A*, 481, 777
- Shkedy Z., Decin L., Molenberghs G., Aerts C., 2007, *MNRAS*, 377, 120
- Stoehr F. et al., 2008, in *Astronomical Society of the Pacific Conference Series*, Vol. 394, *Astronomical Data Analysis Software and Systems XVII*, Argyle R. W., Bunclark P. S., Lewis J. R., eds., p. 505
- Takeda Y., Kambe E., Sadakane K., Masada S., 2010, *PASJ*, 62, 1239
- Trotta R., 2007, *MNRAS*, 378, 72

APPENDIX A: SUPPLEMENTARY FIGURES

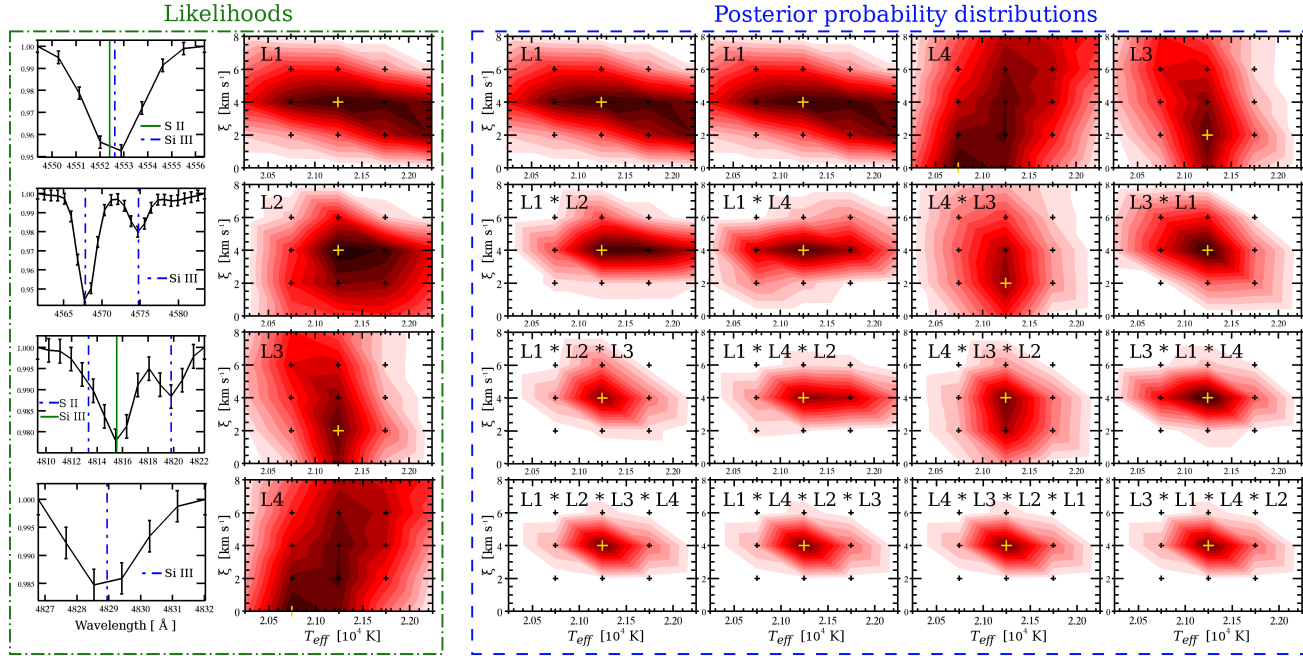


Figure A1. Illustration of the commutativity of the analysis. The lines from Fig 2 are used here with a similar grid of synthetic spectra where all the parameters other than T_{eff} and ξ have been marginalized. The green dash-dotted frame on the left shows each line considered with its respective likelihood, while the blue dashed frames holds the posterior probability distribution obtained when considering several possible combinations of the likelihoods. From the top to the bottom, each column of the blue frame shows the evolution of the posterior probability distribution as new lines are added to the analysis. While the order in which the lines are added differs from column to column, the final posterior probability distribution (bottom row) remains the same in each case. Note that the products written in each graphic (such as $L1*L2*L3$) are simplified for clarity. In fact, each posterior distribution is the normalised product of the likelihoods as stated in equation 9.

APPENDIX B: TABLES OF STELLAR PARAMETERS

Table B1: Basic Parameters of Field B Stars

Star Id.	T_{eff} (K)	$\log(g)$	$v \sin(i)$ (km s ⁻¹)	ξ (km s ⁻¹)	ref
HD886	21250 ± 130	3.98 ± 0.04	31 ⁺⁹ ₋₁₁	8 ± 1	TW
	21600 ± 1000	3.7 ± 0.3	8 ± 2	3.3	AND99
	23000 ± 1000	3.8 ± 0.1	10 ± 1	1 ⁺² ₋₁	LEF10
	21667 ± 650	3.8 ± 0.2	0 ± 9	3 ± 2	TAK10
HD3827	29440 ⁺¹⁷⁰ ₋₂₄₀	4.27 ± 0.04	155 ± 5	6 ± 1	TW
	24678 ± 450	3.836 ± 0.038	164 ± 10	2	HG10
HD5882	18250 ± 130	4.27 ± 0.04	330 ⁺⁵ ₋₁₀	7 ⁺¹ ₋₂	TW
	15626 ± 150	3.731 ± 0.021	358 ± 5	2	HG10
HD32249	20000 ± 130	4.26 ± 0.13	90 ± 10	5 ± 1	TW
	17081 ± 150	3.859 ± 0.025	60 ± 12	2	HG10
	18300 ± 300	3.9 ± 0.1	46	0.5 ⁺⁰ _{-0.5}	LYU05
	18500 ± 1000	4. ± 0.3	48 ± 8	4	AND99
	18890 ± 567	4.1 ± 0.2	30 ± 9	3 ± 2	TAK10
HD32672	20950 ⁺¹³⁰ ₋₁₅₀	3.93 ± 0.04	37 ± 13	4 ⁺¹ ₋₂	TW
	18089 ± 300	3.434 ± 0.034	32 ± 14	2	HG10
HD33816	22430 ⁺³²⁰ ₋₂₄₀	3.94 ± 0.06	8 ⁺¹² ₋₈	7 ± 1	TW
	21613 ± 500	3.818 ± 0.049	24 ± 24	2	HG10
HD35912	19400 ⁺²³⁰ ₋₁₅₀	4.23 ^{+0.08} _{-0.04}	15 ⁺¹⁷ ₋₁₅	1 ⁺² ₋₁	TW
	19000 ± 1000	4.1 ± 0.3	22 ± 4	4	AND99
HD36280	28000 ± 130	4.02 ± 0.04	203 ⁺⁷ ₋₈	9 ⁺² ₋₁	TW
	23611 ± 600	3.613 ± 0.053	206 ± 9	2	HG10
HD37032	30000 ⁺⁰ ₋₂₅₀	4.07 ± 0.04	63 ± 15	10 ⁺¹ ₋₂	TW
	22499 ± 300	3.442 ± 0.028	70 ± 14	2	HG10
HD40160	20010 ⁺²⁹⁰ ₋₂₄₀	4.05 ^{+0.07} _{-0.05}	128 ⁺⁷ ₋₈	5 ⁺¹ ₋₂	TW
	16453 ± 250	3.735 ± 0.027	115 ± 13	2	HG10
HD42782	15000 ⁺²⁵⁰ ₋₀	4.02 ± 0.04	60 ⁺²⁷ ₋₂₁	0 ⁺² ₋₀	TW
	15133 ± 150	3.790 ± 0.023	44 ± 21	2	HG10
HD44700	17380 ± 130	4.24 ± 0.04	28 ⁺¹⁸ ₋₂₂	5 ± 1	TW
	17520 ⁺²³⁰ ₋₁₆₀	4.24 ± 0.13	4 ⁺¹⁰ ₋₄	6 ± 1	TW ¹
	15190 ± 150	3.907 ± 0.026	26 ± 26	2	HG10
	17500 ± 500	3.8 ± 0.1	8 ± 1	6 ± 2	LEF10
	16551 ± 497	4.2 ± 0.2	0 ± 9	3 ± 2	TAK10
HD45418	16750 ± 130	4.27 ± 0.04	247 ⁺⁸ ₋₇	6 ± 1	TW
	16000 ± 500	4. ± 0.2	237 ± 28	3 ± 2	LEF10
HD77770	19250 ± 130	3.77 ± 0.04	14 ⁺⁶ ₋₁₄	7 ± 1	TW
	19000 ± 130	3.53 ± 0.04	0 ⁺¹³ ₋₀	4 ⁺¹ ₋₂	TW ¹
	16935 ± 200	3.386 ± 0.023	49 ± 49	2	HG10
HD160762	17050 ± 200	3.83 ± 0.03	3 ⁺¹² ₋₃	8 ± 1	TW
	17000 ± 250	3.77 ± 0.12	15	1.3 ⁺¹ _{-1.3}	LYU05
	19500 ± 500	4.1 ± 0.1	8 ± 2	3 ± 2	LEF10
	17440 ± 523	3.9 ± 0.2	0 ± 9	3 ± 2	TAK10
HD166182	19130 ⁺¹²⁰ ₋₁₃₀	3.54 ± 0.04	0 ⁺¹⁰ ₋₀	10 ± 1	TW
	20000 ± 600	3.54 ± 0.16	44	4.7 ⁺⁴ _{-4.7}	LYU05
HD184171	16980 ⁺¹⁵⁰ ₋₂₃₀	3.89 ^{+0.05} _{-0.07}	3 ⁺⁷ ₋₃	3 ± 1	TW
	16100 ± 700	3.62 ± 0.15	29	0 ± 0	LYU05
	15858 ± 476	3.5 ± 0.2	15 ± 9	3 ± 2	TAK10

Continued on next page

Table B1 – continued from previous page

Star Id.	T_{eff} (K)	$\log(g)$	$v \sin(i)$ (km s ⁻¹)	ξ (km s ⁻¹)	ref
HD185330	15000 $^{+250}_{-0}$	3.70 ± 0.04	115 $^{+11}_{-10}$	1 ± 1	TW
	16167 ± 485	3.7 ± 0.2	15 ± 9	3 ± 2	TAK10
HD188892	15120 $^{+130}_{-120}$	3.57 ± 0.04	3 $^{+7}_{-3}$	4 ± 1	TW
	14008 ± 420	3.3 ± 0.2	30 ± 9	3 ± 2	TAK10
HD189944	15500 ± 130	4.02 ± 0.04	0 $^{+10}_{-0}$	6 ± 1	TW
	14793 ± 444	4.0 ± 0.2	10 ± 9	3 ± 2	TAK10
HD190066	23560 $^{+190}_{-180}$	2.90 ± 0.04	99 $^{+6}_{-9}$	25 $^{+1}_{-2}$	TW
	21000 ± 1000	2.88 ± 0.25	82 ± 20	15	SEA08
HD191243	15130 $^{+120}_{-130}$	2.73 ± 0.04	3 $^{+7}_{-3}$	11 ± 1	TW
	13923 ± 418	2.5 ± 0.2	30 ± 9	3 ± 2	TAK10
	14500 ± 1000	2.75 ± 0.25	38 ± 20	20	SEA08
	14800 ± 1000	2.6 ± 0.2	38 ± 10	8 ± 5	MAR08
HD192660	25250 ± 130	2.90 ± 0.04	145 ± 5	28 ± 1	TW
	30000 ± 1000	3.25 ± 0.25	94 ± 20	20	SEA08
HD193183	20480 $^{+150}_{-230}$	2.77 $^{+0.04}_{-0.08}$	44 $^{+6}_{-9}$	21 ± 1	TW
	18500 ± 1000	2.63 ± 0.25	68 ± 20	20	SEA08
HD196035	18290 $^{+210}_{-170}$	4.20 ± 0.06	3 $^{+12}_{-3}$	8 ± 1	TW
	17100 ± 250	4.0 ± 0.08	34	2 ± 2	LYU05
	17499 ± 525	4.3 ± 0.2	20 ± 9	3 ± 2	TAK10
HD198478	16380 $^{+120}_{-130}$	2.09 ± 0.04	0 $^{+10}_{-0}$	31 ± 1	TW
	17500 ± 1000	2.25 ± 0.25	61 ± 20	20	SEA08
	17500 ± 1000	2.1 ± 0.2	39 ± 10	8 ± 5	MAR08
HD198820	16760 $^{+120}_{-130}$	3.77 ± 0.04	3 $^{+7}_{-3}$	6 ± 1	TW
	15600 ± 300	3.65 ± 0.15	35	0.1 $^{+0}_{-0.1}$	LYU05
	15852 ± 476	3.8 ± 0.2	15 ± 9	3 ± 2	TAK10
HD199578	15000 $^{+250}_{-0}$	4.05 ± 0.04	3 $^{+7}_{-3}$	5 ± 1	TW
	14480 ± 434	4.0 ± 0.2	30 ± 9	3 ± 2	TAK10
HD202347	22630 $^{+120}_{-130}$	4.08 ± 0.04	95 ± 5	8 ± 1	TW
	23280 ± 900	4.13 ± 0.1	119 ± 6	6 ± 1.5	DAF07
HD205794	27980 $^{+130}_{-120}$	4.17 ± 0.03	5 $^{+25}_{-5}$	9 ± 1	TW
	26890 ± 1000	4.21 ± 0.1	14 ± 3	8 ± 1.5	DAF07
HD206165	19020 $^{+230}_{-150}$	2.59 ± 0.04	75 ± 5	21 ± 1	TW
	18000 ± 1000	2.50 ± 0.25	73 ± 20	15	SEA08
	19300 ± 1000	2.5 ± 0.2	45 ± 10	8 ± 5	MAR08
HD206540	15000 $^{+250}_{-0}$	4.21 ± 0.04	6 $^{+14}_{-6}$	5 ± 1	TW
	13981 ± 419	4.0 ± 0.2	20 ± 9	3 ± 2	TAK10
HD209419	15020 $^{+230}_{-20}$	3.96 $^{+0.07}_{-0.05}$	40 $^{+14}_{-10}$	5 ± 1	TW
	14100 ± 600	3.70 ± 0.12	17	0 ± 0	LYU05
	14404 ± 432	3.8 ± 0.2	20 ± 9	3 ± 2	TAK10
HD213087	24870 $^{+130}_{-120}$	2.90 ± 0.04	103 ± 8	24 ± 1	TW
	27000 ± 1000	3.13 ± 0.25	88 ± 20	20	SEA08
HD214263	20860 $^{+140}_{-240}$	4.15 ± 0.04	90 $^{+5}_{-10}$	6 $^{+1}_{-2}$	TW
	19027 ± 250	3.807 ± 0.025	63 ± 16	2	HG10
HD214432	19500 ± 130	4.49 $^{+0.01}_{-0.05}$	135 ± 5	7 ± 1	TW
	16124 ± 200	3.890 ± 0.028	137 ± 9	2	HG10
HD215191	22010 $^{+240}_{-260}$	4.0 ± 0.06	200 ± 5	8 ± 1	TW
	21487 ± 350	3.83 ± 0.03	195 ± 11	2	HG10

Continued on next page

Table B1 – continued from previous page

Star Id.	T_{eff} (K)	$\log(g)$	$v \sin(i)$ (km s ⁻¹)	ξ (km s ⁻¹)	ref
HD215371	20380 ⁺¹²⁰ ₋₁₃₀	4.27 ± 0.04	165 ± 5	8 ± 1	TW
	17688 ± 250	3.806 ± 0.024	138 ± 10	2	HG10

1: Spectrum with an effective resolution of 0.9 Å.

References: TW = This Work using models from TLUSTY with the solar composition from Asplund et al. (2009);

HG10 = Huang, Gies & McSwain (2010); LEF10 = Lefever et al. (2010); TAK10 = Takeda et al. (2010);

SEA08 = Searle et al. (2008); MAR08 = Markova & Puls (2008); DAF07 = Daflon et al. (2007);

HG06 = Huang & Gies (2006a,b); LYU05 = Lyubimkov et al. (2005); and AND99 = Andrievsky et al. (1999).

Table B2: Basic Parameters of Cluster B Stars

Cluster Id.	Star Id.	T_{eff} (K)	$\log(g)$	$v \sin(i)$ (km s ⁻¹)	ξ (km s ⁻¹)	ref
NGC1960	BD+34 1103s	19660 $^{+220}_{-160}$	4.30 ± 0.04	288 $^{+9}_{-6}$	4 $^{+1}_{-2}$	TW
		17297 ± 150	3.983 ± 0.015	77 ± 7	2	HG10
	SAB20	15000 $^{+250}_{-0}$	4.20 $^{+0.04}_{-0.08}$	301 $^{+11}_{-9}$	6 ± 3	TW
		14845 ± 100	4.242 ± 0.018	141 ± 7	2	HG10
	SAB22	15000 $^{+130}_{-0}$	4.35 ± 0.04	118 $^{+7}_{-8}$	3 $^{+2}_{-1}$	TW
		13579 ± 100	4.071 ± 0.019	135 ± 6	2	HG10
	SAB23	15000 $^{+250}_{-0}$	4.5 $^{+0}_{-0.06}$	300 ± 20	0 $^{+4}_{-0}$	TW
		13715 ± 150	4.267 ± 0.028	302 ± 11	2	HG10
	SAB30	15240 $^{+760}_{-240}$	4.34 $^{+0.16}_{-0.28}$	351 $^{+43}_{-45}$	13 $^{+8}_{-13}$	TW
13651 ± 150		4.07 ± 0.03	79 ± 24	2	HG10	
SAO58227	16870 $^{+130}_{-120}$	4.47 ± 0.03	87 $^{+14}_{-6}$	2 $^{+2}_{-1}$	TW	
	14625 ± 100	4.031 ± 0.017	72 ± 7	2	HG10	
SAO58230	20830 $^{+140}_{-240}$	4.09 ± 0.04	95 $^{+5}_{-10}$	6 ± 1	TW	
	19671 ± 300	3.879 ± 0.026	57 ± 11	2	HG10	
SAO58239	20600 $^{+160}_{-130}$	4.06 ± 0.04	315 ± 5	5 ± 1	TW	
	19582 ± 200	3.911 ± 0.018	199 ± 7	2	HG10	
NGC884	BD+56 556	25130 $^{+140}_{-250}$	3.97 $^{+0.04}_{-0.08}$	140 ± 5	10 ± 1	TW
		25937 ± 401	4.160 ± 0.041	69 ± 9	2	HG06
	BD+56 604	23250 ± 130	3.83 ± 0.04	136 $^{+9}_{-6}$	4 ± 1	TW
		23972 ± 500	3.999 ± 0.048	97 ± 10	2	HG10
	HD14321	22620 $^{+130}_{-250}$	3.77 ± 0.04	150 ± 5	6 ± 1	TW
		23601 ± 550	3.896 ± 0.046	106 ± 10	2	HG10
	HD14476	24630 $^{+120}_{-130}$	3.45 ± 0.04	105 ± 5	13 ± 1	TW
		26006 ± 800	3.749 ± 0.094	40 ± 14	2	HG10
	HG2048	19720 $^{+110}_{-120}$	4.31 ± 0.04	203 $^{+7}_{-8}$	6 $^{+1}_{-2}$	TW
		18007 ± 198	3.944 ± 0.027	125 ± 8	2	HG06
HG2255	21670 $^{+240}_{-140}$	3.83 ± 0.04	329 $^{+6}_{-9}$	6 ± 1	TW	
	20360 ± 178	3.560 ± 0.022	318 ± 10	2	HG06	
HG2794	22510 ± 260	3.78 $^{+0.07}_{-0.05}$	140 ± 10	8 ± 1	TW	
	21624 ± 291	3.611 ± 0.027	79 ± 8	2	HG06	
W168	21370 $^{+130}_{-120}$	4.27 ± 0.04	29 $^{+10}_{-14}$	5 $^{+1}_{-2}$	TW	
	19259 ± 350	3.98 ± 0.04	44 ± 14	2	HG10	

References: TW = This Work using models from TLUSTY with the solar composition from Asplund et al. (2009); HG10 = Huang, Gies & McSwain (2010); and HG06 = Huang & Gies (2006a,b).

Table B3: Basic Parameters of Field B Stars with Modified He and Si Abundances from Lefever et al. (2010)

Star Id.	T_{eff} (K)	$\log(g)$	$v \sin(i)$ (km s⁻¹)	ξ (km s⁻¹)	$\log(\frac{He}{H}) + 12$	$\log(\frac{Si}{H}) + 12$	ref
HD160762	18090 ⁺¹³⁰ ₋₁₂₀	3.97 ± 0.04	$3 \begin{smallmatrix} +7 \\ -3 \end{smallmatrix}$	9 ± 1	11	7.14	TW
	19500 ± 500	4.1 ± 0.1	8 ± 2	3 ± 2			LEF10
HD44700	17250 ± 130	4.22 ± 0.04	$8 \begin{smallmatrix} +16 \\ -8 \end{smallmatrix}$	6 ± 1	11	7.07	TW
	17500 ± 500	3.8 ± 0.1	8 ± 1	6 ± 2			LEF10
HD45418	16750 ± 130	4.27 ± 0.04	$247 \begin{smallmatrix} +8 \\ -7 \end{smallmatrix}$	6 ± 1	11	7.51	TW
	16000 ± 500	$4. \pm 0.2$	237 ± 28	3 ± 2			LEF10
HD886	21120 ⁺¹⁴⁰ ₋₂₄₀	3.95 ± 0.04	34 ± 8	9 ± 1	11	7.16	TW
	23000 ± 1000	3.8 ± 0.1	10 ± 1	$1 \begin{smallmatrix} +2 \\ -1 \end{smallmatrix}$			LEF10

References: TW = This Work; LEF10 = Lefever et al. (2010).

Table B4: Basic Parameters of Field B Stars with Modified O and Ne Abundances from Takeda et al. (2010)

Star Id.	T_{eff} (K)	$\log(g)$	$v \sin(i)$ (km s ⁻¹)	ξ (km s ⁻¹)	$\log(\frac{O}{H}) + 12$	$\log(\frac{Ne}{H}) + 12$	ref
HD160762	16880 ± 130 <i>17440 ± 523</i>	3.81 ± 0.04 <i>3.9 ± 0.2</i>	3 ⁺¹² ₋₃ <i>0 ± 9</i>	8 ⁺¹ ₋₂ <i>3 ± 2</i>	8.74	8.08	TW <i>TAK10</i>
HD184171	17000 ± 130 <i>15858 ± 476</i>	3.86 ± 0.04 <i>3.5 ± 0.2</i>	3 ⁺⁷ ₋₃ <i>15 ± 9</i>	3 ± 1 <i>3 ± 2</i>	8.69	8.01	TW <i>TAK10</i>
HD185330	15000 ⁺²⁵⁰ ₋₀ <i>16167 ± 485</i>	3.70 ± 0.04 <i>3.7 ± 0.2</i>	120 ± 12 <i>15 ± 9</i>	2 ⁺² ₋₁ <i>3 ± 2</i>	8.35	8.15	TW <i>TAK10</i>
HD188892	15120 ⁺¹³⁰ ₋₁₂₀ <i>14008 ± 420</i>	3.57 ± 0.04 <i>3.3 ± 0.2</i>	3 ⁺⁷ ₋₃ <i>30 ± 9</i>	4 ± 1 <i>3 ± 2</i>	8.67	8.01	TW <i>TAK10</i>
HD189944	15500 ± 130 <i>14793 ± 444</i>	4.02 ± 0.04 <i>4.0 ± 0.2</i>	0 ⁺¹⁰ ₋₀ <i>10 ± 9</i>	6 ± 1 <i>3 ± 2</i>	8.79	8.11	TW <i>TAK10</i>
HD191243	15230 ⁺¹⁵⁰ ₋₂₃₀ <i>13923 ± 418</i>	2.76 ^{+0.05} _{-0.07} <i>2.5 ± 0.2</i>	3 ⁺⁷ ₋₃ <i>30 ± 9</i>	10 ⁺² ₋₁ <i>3 ± 2</i>	8.66	7.95	TW <i>TAK10</i>
HD196035	18350 ⁺¹⁰⁰ ₋₁₁₀ <i>17499 ± 525</i>	4.20 ± 0.03 <i>4.3 ± 0.2</i>	3 ⁺¹² ₋₃ <i>20 ± 9</i>	8 ⁺¹ ₋₂ <i>3 ± 2</i>	8.7	8.08	TW <i>TAK10</i>
HD198820	16750 ⁺¹³⁰ ₋₁₂₀ <i>15852 ± 476</i>	3.77 ± 0.04 <i>3.8 ± 0.2</i>	3 ⁺⁷ ₋₃ <i>15 ± 9</i>	6 ± 1 <i>3 ± 2</i>	8.8	8.13	TW <i>TAK10</i>
HD199578	15000 ⁺²⁵⁰ ₋₀ <i>14480 ± 434</i>	4.05 ± 0.04 <i>4.0 ± 0.2</i>	3 ⁺⁷ ₋₃ <i>30 ± 9</i>	6 ⁺¹ ₋₂ <i>3 ± 2</i>	8.7	8.14	TW <i>TAK10</i>
HD206540	15000 ⁺²⁵⁰ ₋₀ <i>13981 ± 419</i>	4.21 ^{+0.07} _{-0.05} <i>4.0 ± 0.2</i>	4 ⁺¹⁶ ₋₄ <i>20 ± 9</i>	4 ± 1 <i>3 ± 2</i>	8.72	8	TW <i>TAK10</i>
HD209419	15000 ⁺¹³⁰ ₋₀ <i>14404 ± 432</i>	3.95 ± 0.04 <i>3.8 ± 0.2</i>	41 ⁺¹⁰ ₋₁₁ <i>20 ± 9</i>	5 ± 1 <i>3 ± 2</i>	8.73	7.99	TW <i>TAK10</i>
HD32249	19980 ⁺¹³⁰ ₋₁₂₀ <i>18890 ± 567</i>	4.26 ± 0.13 <i>4.1 ± 0.2</i>	86 ± 8 <i>30 ± 9</i>	5 ± 1 <i>3 ± 2</i>	8.69	7.95	TW <i>TAK10</i>
HD44700	17370 ⁺¹³⁰ ₋₁₂₀ <i>16551 ± 497</i>	4.24 ± 0.04 <i>4.2 ± 0.2</i>	29 ± 10 <i>0 ± 9</i>	5 ± 1 <i>3 ± 2</i>	8.73	8.04	TW <i>TAK10</i>
HD886	20930 ⁺¹⁴⁰ ₋₁₅₀ <i>21667 ± 650</i>	3.95 ± 0.04 <i>3.8 ± 0.2</i>	31 ⁺⁹ ₋₁₁ <i>0 ± 9</i>	8 ± 1 <i>3 ± 2</i>	8.77	8.09	TW <i>TAK10</i>

References: TW = This Work; TAK10 = Takeda et al. (2010).

Table B5: Basic Parameters of Field B Stars with Modified C, N, O Abundances from Searle et al. (2008)

Star Id.	T_{eff} (K)	$\log(g)$	$v \sin(i)$ (km s ⁻¹)	ξ (km s ⁻¹)	$\log(\frac{C}{H}) + 12$	$\log(\frac{N}{H}) + 12$	$\log(\frac{O}{H}) + 12$	ref
HD190066	23750 ± 190 21000 ± 1000	2.90 ± 0.04 2.88 ± 0.25	95 ± 9 82 ± 20	25 ± 1 15	7.88	8.15	8.53	TW SEA08
HD191243	15120 ⁺¹³⁰ / ₋₁₂₀ 14500 ± 1000	2.70 ± 0.04 2.75 ± 0.25	3 ⁺⁷ / ₋₃ 38 ± 20	11 ± 1 20	7.70	7.65		TW SEA08
HD192660	25140 ± 160 30000 ± 1000	2.88 ± 0.03 3.25 ± 0.25	140 ± 5 94 ± 20	29 ⁺¹ / ₋₂ 20	8.02	7.51	8.73	TW SEA08
HD193183	19610 ⁺¹⁴⁰ / ₋₂₄₀ 18500 ± 1000	2.65 ± 0.04 2.63 ± 0.25	32 ± 12 68 ± 20	23 ± 1 20	7.66	8.15	8.73	TW SEA08
HD198478	16130 ⁺¹²⁰ / ₋₁₃₀ 17500 ± 1000	2.04 ± 0.04 2.25 ± 0.25	0 ⁺¹⁰ / ₋₀ 61 ± 20	33 ± 1 20	7.86	8.29	8.45	TW SEA08
HD206165	18630 ⁺¹²⁰ / ₋₁₃₀ 18000 ± 1000	2.55 ± 0.04 2.50 ± 0.25	75 ± 5 73 ± 20	23 ± 1 15	7.96	8.15	8.43	TW SEA08
HD213087	24620 ⁺¹³⁰ / ₋₁₂₀ 27000 ± 1000	2.86 ± 0.04 3.13 ± 0.25	103 ± 8 88 ± 20	24 ± 1 20	8.00	8.15	8.73	TW SEA08

References: TW = This Work; SEA08 = Searle et al. (2008).

Table B6: Basic Parameters of Field B Stars with Modified He and Si Abundances from Markova & Puls (2008)

Star Id.	T_{eff} (K)	$\log(g)$	$v \sin(i)$ (km s ⁻¹)	ξ (km s ⁻¹)	$\log(\frac{He}{H}) + 12$	$\log(\frac{Si}{H}) + 12$	ref
HD191243	15240 ⁺¹⁴⁰ / ₋₂₄₀ 14800 ± 1000	2.77 ^{+0.04} / _{-0.08} 2.6 ± 0.2	3 ⁺⁷ / ₋₃ 38 ± 10	11 ± 1 8 ± 5	10.954	7.48	TW MAR08
HD198478	16270 ⁺²³⁰ / ₋₁₅₀ 17500 ± 1000	2.08 ^{+0.08} / _{-0.04} 2.1 ± 0.2	2 ⁺²⁸ / ₋₂ 39 ± 10	26 ⁺¹ / ₋₂ 8 ± 5	11.176	7.58	TW MAR08
HD206165	19380 ⁺¹²⁰ / ₋₁₃₀ 19300 ± 1000	2.63 ± 0.04 2.5 ± 0.2	76 ⁺⁹ / ₋₆ 45 ± 10	16 ⁺² / ₋₁ 8 ± 5	11.176	7.58	TW MAR08

References: TW = This Work; MAR08 = Markova & Puls (2008).

Table B7: Basic Parameters of Field B Stars with Modified C, N, O, Mg, Al, and Si Abundances from Daflon et al. (2007)

Star Id.	T_{eff} (K)	$\log(g)$	$v \sin(i)$ (km s ⁻¹)	ξ (km s ⁻¹)	$\epsilon(C)$	$\epsilon(N)$	$\epsilon(O)$	$\epsilon(Mg)$	$\epsilon(Al)$	$\epsilon(Si)$	ref
hd202347	23730 $^{+240}_{-260}$ <i>23280 ± 900</i>	4.27 $^{+0.04}_{-0.08}$ <i>4.1 ± 0.1</i>	96 $^{+9}_{-6}$ <i>119 ± 6</i>	9 ± 1 <i>6 $^{+1}_{-1.5}$</i>		7.54	8.54	7.35	6.28	7.13	TW <i>DAF07</i>
hd205794	25010 $^{+120}_{-130}$ <i>26890 ± 1000</i>	3.95 ± 0.04 <i>4.2 ± 0.1</i>	3 $^{+17}_{-3}$ <i>14 ± 3</i>	11 ± 1 <i>8 $^{+1}_{-1.5}$</i>	8.09	7.57	8.63			7.09	TW <i>DAF07</i>

References: TW = This Work; AND99 = Daflon et al. (2007). Here, $\epsilon(X) = \log(X/H) + 12$.

Table B8: Basic Parameters of Field B Stars with Modified He and Mg Abundances from Lyubimkov et al. (2005)

Star Id.	T_{eff} (K)	$\log(g)$	$v \sin(i)$ (km s ⁻¹)	ξ (km s ⁻¹)	$\log(\frac{He}{H}) + 12$	$\log(\frac{Mg}{H}) + 12$	ref
HD160762	17280 $^{+120}_{-130}$ <i>17000 ± 250</i>	3.88 ± 0.04 <i>3.77 ± 0.12</i>	3 $^{+7}_{-3}$ <i>15</i>	7 ± 1 <i>1.3 $^{+1}_{-1.3}$</i>	11.057	7.62	TW <i>LYU05</i>
HD166182	19150 $^{+230}_{-150}$ <i>20000 ± 600</i>	3.55 $^{+0.07}_{-0.05}$ <i>3.54 ± 0.16</i>	0 $^{+10}_{-0}$ <i>44</i>	9 ± 1 <i>4.7 $^{+4}_{-4.7}$</i>	11.045	7.39	TW <i>LYU05</i>
HD184171	16880 $^{+120}_{-130}$ <i>16100 ± 700</i>	3.85 ± 0.04 <i>3.62 ± 0.15</i>	3 $^{+7}_{-3}$ <i>29</i>	2 ± 1 <i>0 ± 0</i>	11.041	7.89	TW <i>LYU05</i>
HD196035	18210 $^{+170}_{-210}$ <i>17100 ± 250</i>	4.18 ± 0.04 <i>4.0 ± 0.08</i>	3 $^{+7}_{-3}$ <i>34</i>	6 $^{+2}_{-1}$ <i>2 ± 2</i>	11.065	7.66	TW <i>LYU05</i>
HD198820	16500 ± 130 <i>15600 ± 300</i>	3.73 ± 0.04 <i>3.65 ± 0.15</i>	3 $^{+7}_{-3}$ <i>35</i>	3 ± 1 <i>0.1 $^{+0}_{-0.1}$</i>	11.11	8.01	TW <i>LYU05</i>
HD209419	15000 $^{+250}_{-0}$ <i>14100 ± 600</i>	3.95 ± 0.04 <i>3.70 ± 0.12</i>	60 ± 5 <i>17</i>	4 ± 1 <i>0 ± 0</i>	11.093	8.03	TW <i>LYU05</i>
HD32249	18880 $^{+120}_{-130}$ <i>18300 ± 300</i>	4.11 ± 0.04 <i>3.9 ± 0.1</i>	90 ± 5 <i>46</i>	2 ± 1 <i>0.5 $^{+0}_{-0.5}$</i>	11.124	8.02	TW <i>LYU05</i>

References: TW = This Work; LYU05 = Lyubimkov et al. (2005).

Table B9: Basic Parameters of Field B Stars with Modified C and N Abundances from Andrievsky et al. (1999)

Star Id.	T_{eff} (K)	$\log(g)$	$v \sin(i)$ (km s ⁻¹)	ξ (km s ⁻¹)	$\log(\frac{C}{H}) + 12$	$\log(\frac{N}{H}) + 12$	ref
HD32249	20000 ± 130 <i>18500 ± 1000</i>	4.26 ± 0.13 <i>4. ± 0.3</i>	86 ⁺¹¹ ₋₇ <i>48 ± 8</i>	5 ± 1 <i>4</i>	8.19	7.8	TW <i>AND99</i>
HD35912	19610 ⁺¹⁴⁰ ₋₂₄₀ <i>19000 ± 1000</i>	4.27 ± 0.04 <i>4.1 ± 0.3</i>	17 ⁺¹⁵ ₋₁₇ <i>22 ± 4</i>	1 ⁺² ₋₁ <i>4</i>	8.28	7.76	TW <i>AND99</i>
HD886	21250 ± 130 <i>21600 ± 1000</i>	3.97 ± 0.04 <i>3.7 ± 0.3</i>	4 ⁺¹⁶ ₋₄ <i>8 ± 2</i>	8 ± 1 <i>3.3</i>	8.11	7.55	TW <i>AND99</i>

References: TW = This Work; AND99 = Andrievsky et al. (1999).

Table B10: Basic Parameters of Field B Stars Returned by ATLAS9 with Solar Composition from Grevesse & Sauval (1998)

Star Id.	T_{eff} (K)	$\log(g)$	$v \sin(i)$ (km s ⁻¹)	ξ (km s ⁻¹)	ref
HD214263 (16)	19760 ⁺¹²⁰ ₋₁₄₀ <i>18570 ± 350</i> <i>19027 ± 250</i>	4.08 ± 0.04 <i>3.87 ± 0.06</i> <i>3.807 ± 0.025</i>	88 ⁺⁷ ₋₈ <i>63</i> <i>63 ± 16</i>	1 ⁺² ₋₁ <i>2</i> <i>2</i>	TW <i>TWHG</i> <i>HG10</i>
HD214432 (17)	18870 ⁺¹³⁰ ₋₁₂₀ <i>15560 ⁺⁴⁵⁰₋₅₆₀</i> <i>16124 ± 200</i>	4.47 ± 0.04 <i>3.95 ± 0.08</i> <i>3.890 ± 0.028</i>	132 ⁺⁸ ₋₇ <i>137</i> <i>137 ± 9</i>	5 ± 1 <i>2</i> <i>2</i>	TW <i>TWHG</i> <i>HG10</i>
HD215191 (18)	20500 ⁺¹³⁰ ₋₁₂₀ <i>20490 ± 360</i> <i>21487 ± 350</i>	3.91 ± 0.04 <i>3.88 ± 0.06</i> <i>3.83 ± 0.03</i>	200 ± 5 <i>195</i> <i>195 ± 11</i>	6 ± 1 <i>2</i> <i>2</i>	TW <i>TWHG</i> <i>HG10</i>
HD215371 (19)	19380 ⁺²⁴⁰ ₋₁₄₀ <i>18131 ± 450</i> <i>17688 ± 250</i>	4.23 ± 0.04 <i>3.99 ± 0.1</i> <i>3.806 ± 0.024</i>	160 ± 5 <i>138</i> <i>138 ± 10</i>	5 ± 1 <i>2</i> <i>2</i>	TW <i>TWHG</i> <i>HG10</i>
HD32249 (20)	18890 ± 130 <i>16490 ± 450</i> <i>17081 ± 150</i>	4.25 ± 0.04 <i>3.84 ± 0.11</i> <i>3.859 ± 0.025</i>	95 ± 5 <i>60</i> <i>60 ± 12</i>	4 ± 1 <i>2</i> <i>2</i>	TW <i>TWHG</i> <i>HG10</i>
HD32672 (21)	19770 ⁺⁴⁰⁰ ₋₂₅₀ <i>18290 ± 570</i> <i>18089 ± 300</i>	3.87 ^{+0.07} _{-0.05} <i>3.69 ± 0.08</i> <i>3.434 ± 0.034</i>	18 ⁺²² ₋₁₈ <i>32</i> <i>32 ± 14</i>	1 ± 1 <i>2</i> <i>2</i>	TW <i>TWHG</i> <i>HG10</i>
HD33816 (22)	20780 ⁺¹³⁰ ₋₁₄₀ <i>21110 ± 1540</i> <i>21613 ± 500</i>	3.85 ± 0.04 <i>3.91 ± 0.06</i> <i>3.818 ± 0.049</i>	8 ⁺¹² ₋₈ <i>24</i> <i>24 ± 24</i>	4 ± 1 <i>2</i> <i>2</i>	TW <i>TWHG</i> <i>HG10</i>
HD36280 (23)	24330 ⁺¹⁶⁰ ₋₁₇₀ <i>24020 ± 530</i> <i>23611 ± 600</i>	3.91 ± 0.04 <i>3.84 ± 0.1</i> <i>3.613 ± 0.053</i>	214 ± 6 <i>206</i> <i>206 ± 9</i>	8 ± 1 <i>2</i> <i>2</i>	TW <i>TWHG</i> <i>HG10</i>
HD37032 (24)	29540 ⁺²⁴⁰ ₋₂₉₀ <i>22110 ± 1300</i> <i>22499 ± 300</i>	4.28 ^{+0.07} _{-0.05} <i>3.56 ± 0.17</i> <i>3.442 ± 0.028</i>	43 ⁺¹⁹ ₋₁₁ <i>70</i> <i>70 ± 14</i>	5 ± 1 <i>2</i> <i>2</i>	TW <i>TWHG</i> <i>HG10</i>
HD3827 (25)	29500 ± 500 <i>24100 ± 810</i> <i>24678 ± 450</i>	4.43 ± 0.04 <i>3.93 ± 0.14</i> <i>3.836 ± 0.038</i>	165 ± 5 <i>164</i> <i>164 ± 10</i>	6 ± 1 <i>2</i> <i>2</i>	TW <i>TWHG</i> <i>HG10</i>

Continued on next page

Table B10 – continued from previous page

Star Id.	T_{eff} (K)	$\log(g)$	$v \sin(i)$ (km s ⁻¹)	ξ (km s ⁻¹)	ref
HD42782	13040 ⁺²¹⁰ ₋₁₇₀	3.72 ^{+0.07} _{-0.05}	155 ⁺¹⁷ ₋₁₅	0 ⁺² ₋₀	TW
(26)	14570 ± 590	3.9 ± 0.16	44	2	TWHG
	15133 ± 150	3.790 ± 0.023	44 ± 21	2	HG10
HD44700	16900 ⁺²⁶⁰ ₋₁₅₀	4.23 ^{+0.08} _{-0.04}	82 ⁺⁸ ₋₇	3 ⁺² ₋₁	TW
(27)	15010 ± 510	3.91 ± 0.12	26	2	TWHG
	15190 ± 150	3.907 ± 0.026	26 ± 26	2	HG10
HD5882	17500 ± 130	4.27 ± 0.04	328 ± 6	6 ± 3	TW
(28)	14760 ± 300	3.71 ± 0.09	358	2	TWHG
	15626 ± 150	3.731 ± 0.021	358 ± 5	2	HG10
HD77770	18500 ± 130	3.78 ± 0.04	15 ⁺⁵ ₋₁₀	0 ⁺¹ ₋₀	TW
(29)	15590 ± 420	3.31 ± 0.07	49	2	TWHG
	16935 ± 200	3.386 ± 0.023	49 ± 49	2	HG10

References: TW = This Work; TWHG = This Work using H γ only;
 HG10 = Huang, Gies & McSwain (2010).
 Numbers between parenthesis refer to the 'Star id n°' in Figure 15.

Table B11: Stellar Parameters of Cluster B Stars Returned by ATLAS9 with Solar Composition from Grevesse & Sauval (1998)

Cluster Id.	Star Id.	T_{eff} (K)	$\log(g)$	$v \sin(i)$ (km s ⁻¹)	ξ (km s ⁻¹)	ref
NGC1960	BD341103s (0)	18870 ⁺¹³⁰ ₋₁₂₀	4.31 ± 0.04	290 ⁺⁹ ₋₆	2 ± 1	TW
		20030 ± 920	4.40 ± 0.17	77	2	TWHG
		17297 ± 150	3.983 ± 0.015	77 ± 7	2	HG10
SAB20	(8)	12970 ⁺¹⁵⁰ ₋₂₅₀	3.87 ^{+0.05} _{-0.07}	274 ⁺¹⁴ ₋₁₀	1 ⁺² ₋₁	TW
		14560 ± 620	4.25 ± 0.15	141	2	TWHG
		14845 ± 100	4.242 ± 0.018	141 ± 7	2	HG10
SAB22	(9)	14500 ± 130	4.33 ± 0.04	126 ⁺¹⁰ ₋₅	3 ± 1	TW
		13500 ± 210	4.09 ± 0.06	135	2	TWHG
		13579 ± 100	4.071 ± 0.019	135 ± 6	2	HG10
SAB23	(10)	12780 ⁺²⁷⁰ ₋₁₃₀	4.07 ^{+0.13} _{-0.08}	244 ⁺¹⁶ ₋₁₄	4 ± 2	TW
		12910 ± 1220	4.18 ± 0.3	302	2	TWHG
		13715 ± 150	4.267 ± 0.028	302 ± 11	2	HG10
SAB30	(11)	11920 ⁺⁷¹⁰ ₋₈₂₀	4.89 ^{+0.11} _{-0.19}	261 ⁺³⁷ ₋₅₀	12 ± 3	TW
		12160 ± 840	4.88 ± 0.3	79	2	TWHG
		13651 ± 150	4.07 ± 0.03	79 ± 24	2	HG10
SAO58227	(12)	16600 ⁺¹⁵⁰ ₋₂₃₀	4.52 ^{+0.05} _{-0.07}	123 ⁺⁷ ₋₁₁	5 ± 1	TW
		14790 ± 250	4.19 ± 0.08	72	2	TWHG
		14625 ± 100	4.031 ± 0.017	72 ± 7	2	HG10
SAO58230	(13)	20190 ⁺²⁰⁰ ₋₁₈₀	4.11 ± 0.04	98 ± 12	2 ⁺² ₋₁	TW
		19420 ± 630	4.05 ± 0.1	57	2	TWHG
		19671 ± 300	3.879 ± 0.026	57 ± 11	2	HG10
SAO58239	(14)	19120 ⁺¹³⁰ ₋₁₂₀	3.95 ± 0.04	315 ± 5	2 ± 1	TW
		21000 ± 560	4.15 ± 0.08	199	2	TWHG
		19582 ± 200	3.911 ± 0.018	199 ± 7	2	HG10

Continued on next page

Table B11 – continued from previous page

Cluster Id.	Star Id.	T_{eff} (K)	$\log(g)$	$v \sin(i)$ (km s ⁻¹)	ξ (km s ⁻¹)	ref
NGC884	BD56556 (1)	24390 ⁺²³⁰ ₋₁₄₀	3.87 ^{+0.07} _{-0.05}	145 ± 5	9 ± 1	TW
		25000 ± 2300	4.25 ± 0.25	69	2	TWHG
		25937 ± 401	4.160 ± 0.041	69 ± 9	2	HG06
	BD56604 (2)	22470 ⁺¹²⁰ ₋₁₄₀	3.86 ± 0.04	150 ± 5	5 ± 1	TW
		24960 ± 880	4.33 ± 0.12	97	2	TWHG
		23972 ± 500	3.999 ± 0.048	97 ± 10	2	HG10
	HD14321 (3)	21750 ± 130	3.73 ± 0.04	150 ± 5	6 ± 1	TW
		22470 ± 1030	3.81 ± 0.14	106	2	TWHG
		23601 ± 550	3.896 ± 0.046	106 ± 10	2	HG10
	HD14476 (4)	25400 ⁺²³⁰ ₋₁₅₀	3.73 ± 0.04	92 ± 5	8 ± 1	TW
		26870 ± 1620	3.96 ± 0.23	40	2	TWHG
		26006 ± 800	3.749 ± 0.094	40 ± 14	2	HG10
	HG2048 (5)	18870 ± 130	4.27 ± 0.04	199 ± 5	4 ⁺² ₋₁	TW
		19530 ± 510	4.30 ± 0.08	125	2	TWHG
		18007 ± 198	3.944 ± 0.027	125 ± 8	2	HG06
HG2255 (6)	19670 ± 170	3.70 ± 0.04	329 ⁺⁶ ₋₉	4 ⁺² ₋₁	TW	
	21220 ± 760	3.89 ± 0.12	318	2	TWHG	
	20360 ± 178	3.560 ± 0.022	318 ± 10	2	HG06	
HG2794 (7)	21500 ± 130	3.77 ± 0.04	148 ⁺⁷ ₋₈	8 ± 1	TW	
	22410 ± 1060	3.94 ± 0.21	79	2	TWHG	
	21624 ± 291	3.611 ± 0.027	79 ± 8	2	HG06	
W168 (15)	19790 ⁺¹²⁰ ₋₁₃₀	4.11 ± 0.04	41 ⁺¹¹ ₋₁₃	1 ± 1	TW	
	18870 ± 680	4.00 ± 0.08	44	2	TWHG	
	19259 ± 350	3.98 ± 0.04	44 ± 14	2	HG10	

References: TW = This Work; TWHG = This Work using H γ only;
 HG10 = Huang, Gies & McSwain (2010); and HG06 = Huang & Gies (2006a,b).
 Numbers between parenthesis refer to the 'Star id n' in Figure 15.